NOVA SCHOOL OF SCIENCE & TECHNOLOGY

DEPARTMENT OF MATERIALS SCIENCE

MARGARIDA ROSADO BARBOSA

Bachelor in ⟨Materials Science and Engineering⟩

MULTILAYER COATINGS FOR TEMPERATURE MANAGEMENT THROUGH GLASS WINDOWS OF BUILDINGS

MATERIALS ENGINEERING

NOVA University Lisbon

⟨June⟩, ⟨2022⟩

NOVA SCHOOL OF
SCIENCE & TECHNOLOGY

DEPARTMENT OF
MATERIALS SCIENCE

MULTILAYER COATINGS FOR TEMPERATURE MANAGEMENT THROUGH GLASS WINDOWS OF BUILDINGS

MARGARIDA ROSADO BARBOSA

Bachelor in ⟨Materials Science and Engineering⟩

Adviser: Ana Cláudia Lourenço Santana Marques
NOVA University of Lisbon, Researcher

Co-adviser: Isabel Maria Mercês Ferreira
NOVA University of Lisbon, Associate Professor

MATERIALS ENGINEERING

NOVA University Lisbon
⟨June⟩, ⟨2022⟩

Multilayer Coatings for temperature management through glass windows of buildings

“Just because you’re trash doesn’t mean you can’t do great things. It’s called garbage can, not garbage cannot.” - Oscar the Grouch.

Acknowledgements

First and foremost, I'd want to express my gratitude to Professor Isabel Ferreira and Ana Marques for welcoming me, for all of the knowledge they shared with me, and for the wonderful opportunity to complete my master's thesis. I'd also like to express my gratitude to everyone in the lab who has assisted me with my work and made my day better.

To my colleagues and friends at FCT/UNL, thank you for being there for me over the last five years, for helping me grow as a person and a professional, and for your patience and support.

I'm also grateful for my mother's unwavering support. Thank you for believing in me and for being such an excellent role model.

“You cannot teach a man anything; you can only help him discover it in himself.” (Galileo)

Abstract

Infrared (IR) blocking windows are considered to have an important role in reducing the building's energy consumption by providing better insulation due to their transparency to visible light and ability to block heat. This work reports on visible light transmitting IR filters formed by a metallic layer between transparent conductive oxides (TCO). GZO as TCO and Cu as the metal layer were the focus of this work. Copper-based low-emissivity coatings are being considered as an alternative to that of Ag due to their lower cost and durability for heat reflectors. The TCOs were deposited by sputtering and the metallic layer by resistive thermal evaporation. Depending on the TCO required thickness (from 20 to 269 nm), different deposition times and powers were used and their influence on the optical properties studied. Results showed that the GZO (20 nm)/Metal/GZO (20 nm) multilayers obtained a transmittance at 550 nm of about 78.1% and 63.1% and a NIR reflection of 80.1% and 72.7% for the Ag (11 nm) and Cu (5 nm), respectively. The best performance was accomplished with the GZO (20 nm)/Ag (11 nm)/GZO (20 nm) film.

CuS or Ag_2S nanoparticles have been added to the coatings as an attempt to absorb NIR radiation and achieve IR-shielding. These have been synthetized by microwave-assisted synthesis (MW) and Ag_2S also via ultrasonic irradiation (UI). Their optical characteristics were obtained before and after deposition on GZO substrates and GZO-metal structures by electrospray. The optical properties revealed that adding those nanoparticles causes the metal films to lose their IR reflective properties and some visible transmission.

Keywords: Infrared, Sputtering, TCO, Metal, Electrospray, Chalcogenides

Resumo

As janelas que bloqueiam os infravermelhos (IR) têm um papel importante na redução do consumo energético dos edifícios, pois proporcionam um melhor isolamento devido à transparência à luz visível e capacidade de bloquear o calor. Este trabalho relata os filtros IR de transmissão de luz visível formados por uma camada metálica entre óxidos condutores transparentes (TCO). O foco incidiu no GZO como TCO e Cu como camada metálica. Os revestimentos de baixa emissividade à base de cobre estão a ser considerados uma alternativa aos de Ag devido ao seu menor custo e durabilidade para refletores de calor. Os TCO foram depositados por pulverização catódica e a camada metálica por evaporação térmica resistiva. Dependendo da espessura do TCO pretendida (entre 20 e 269 nm), foram utilizados diferentes tempos e potências de deposição e estudada a sua influência nas propriedades ópticas. Os resultados mostraram que as multicamadas GZO (20 nm)/Metal/GZO (20 nm) obtiveram uma transmitância nos 550 nm de cerca de 78.1% e 63.1% e uma reflexão no NIR de 80.1% e 72.7% para o Ag (11 nm) e Cu (5 nm), respetivamente. O melhor desempenho foi obtido com o filme GZO (20 nm)/Ag (11 nm)/GZO (20 nm).

As nanopartículas CuS ou Ag_2S foram adicionadas aos revestimentos como uma tentativa de absorver a radiação NIR e conseguir uma proteção IR. Estas foram obtidos por síntese assistida por micro-ondas (MW) e o Ag_2S ainda por irradiação ultrassónica (UI). As suas características ópticas foram obtidas antes e após as deposições por electrospray em substratos GZO e estruturas GZO-metal. No que respeita às propriedades óticas, a adição das nanopartículas fez com que as películas metálicas perdessem as suas propriedades refletoras do IR e alguma transmissão visível.

Palavras-chave: Infravermelho, Pulverização catódica, TCO, Metal, *Electrospray*, Calcogénios

Contents

List of Figures

List of Tables

Glossary

ε Emissivity

A Absorption

ES Electrospray

IR Infrared

Low-e Low emissivity

LSPR Localized surface plasmon resonance

MW Microwave

NIR Near-infrared

NP Nanoparticles

R Reflectance

SPR Surface plasmon resonance

T Transmittance

TCO Transparent conductive oxide

Tvis Visible transmittance

UI Ultrasonic irradiation

1 Introduction

1.1 Context

Since almost 50% of the EU's final energy consumption is used for heating and cooling, with buildings accounting for 80%, priority must be given to energy efficiency [1]. There is a need to increase windows' thermal efficiency seeing they're responsible for a large amount of the heat exchange between the building and the outside. Considering that infrared (IR) radiation is a substantial contributor to heat loss, near-infrared (NIR) radiation shielding is a critical aspect to be explored in the development of energy-saving windows [2]. In addition, the decrease in visible light transmittance would lead to an increased demand for artificial lighting, thereby increasing energy consumption. Therefore, one cost-effective way to control heat transfer, either in to or out of a building, to save heating/cooling energy is through low-emissivity (Low-e) coatings, *i.e.*, coatings with high NIR reflectance and high visible transmittance (Tvis) [3]. Another type of IR-shielding material is NIR absorptive material used in solar-thermal energy conversion [4].

1.2 Low Emissivity Coatings

The material's ability to emit energy as thermal radiation is measured by its emissivity (ε), meaning that highly IR reflective materials have low ε values. The ε of a black-body is 1, while that of a perfect reflector is 0 [5]. Low-e coatings can be classified into two wide categories depending on the wavelength at which the transition from high transmittance to high reflectance takes place (λ_T) [6]. Those intended for solar control, with λ_T<1 μm , reflect the NIR solar radiation (about 50% of the overall solar radiation [7]) and are suitable for warm climates. Those intended for thermal insulation, with λ_T>1 μm, allow some of the sun's shortwave IR to pass through to let as much solar heat as possible into the room in cold climates where solar gains are preferred [6]. Therefore, geographical climate factors are a major aspect to consider for low-e materials: choosing a window with a low-e coating with an unsuitable solar heat gain coefficient (SHGC) could neutralize the potential energy gains [3].

Glass coatings capable of selectively reflecting radiation date back to 1958, when gold based coatings on glass with high-transmittance and high-heat reflection were investigated by Holland and Siddall [8]. In the 1980s, a breakthrough was achieved in a silver coating, with higher transmittance, much lower emissivity, and friendly color [2]. Among the possible metal layer materials Ag, Au, Cu, and Al [9], silver is preferred first for its low resistance and high transmittance from visible light to NIR, but also for its well-developed preparation approaches [10]. This is the most popular material employed in energy saving field, given the thin silver film key properties in low-e coating technology. In fact, in 2017 silver-based low-e window coatings accounted for 90% of the market [2]. That said, Cu based films are establishing themselves as a reliable low cost and durable heat reflecting materials [5, 11]. Therefore, this research line was further exploited in the scope of this thesis.

Current industrial production of low-e films is dominated by multi-layered sputtering system, due to their extremely low, better optical performance, heat radiation control and affordability. Saint Gobain Glass, Pilkington, AGC, LLumar window film are some of the films in this market, all commonly transparent to visible light (45%<Tvis<85%) and UV and IR reflective [5]. Jelle, Kalnæs, and Gao [3] have more detailed information about market products and for a brief history of low-e technology consult [2, 5]. The ε of standard clear glass is about 0.84 for the long-wave part of the spectrum (84% of the solar energy is absorbed and emitted from the glass while only 16% of IR radiation is reflected) [3], but with silver-based sputter

coatings emissivity 8–2% is achievable [2]. It is possible to develop low-e coatings with double or triple silver layers as an inserted layer of the multilayer structure to decrease the emissivity [2, 12]. While double or triple Ag layers can contribute to greater energy efficiency than single low-e glass, due to their higher price as a consequence of the high consumption of Ag, they were not commonly used [12].

Commercially, the silver films glass coating is usually in the range 8-16 nm thickness [13]. However, metal films do not have high enough visible transmission and are unstable under environmental conditions, e.g., are easily oxidized which significantly increases IR emissivity, losing thermal insulation effect. For that reason, a top layer such as dielectric should be applied on the metal layer [6, 14, 15]. Multilayers are usually used for improvement of single thin layer properties to get the best performance for a specific application [6]. For example, the visible transmittance of the Ag/M-Seed/AZO/glass configuration varies from 54% to 66%. By coating the anti-reflective and wide-band dielectric layer(s) on the Ag layer, their visible transmission can be improved, over 80% [13]. Actually, among the possible designs, the dielectric/metal/dielectric (D/M/D) showed in Figure 1.1 is considered to have the best heat reflecting performances [5] as verified by various authors [9, 15, 16]. In short, this design enables the coating protection and enhancement of visible transmission without reducing IR reflection [5]. The overcoat layer serves as anti-reflecting coating to increase visible transmission while protecting the metal layer from the environment [6, 13]. The undercoat layer improves adhesion between glass and metal layer and also plays an antireflective role [5, 16]. As such, the D/M/D based multilayer structure specifically focused on infrared reflection has been extensively studied (M'=Ag, Cu): ZnO/Ag/ZnO [6, 10]; AZO/M'/AZO [15–17]; TiO_2 /M'/TiO_2 [11, 18]; WO_3 /Au/WO_3 [19]; V_2O_5 /Ag/V_2O_5 [20], among others. Transition-metal nitrides (TiN and ZrN) are also considered as an alternative to noble metal layers in the D/M/D structure as they combine promising optical properties with excellent mechanical, thermal, and chemical properties [5, 21].

Besides the metal based multilayer coatings, there is another major kind of transparent heat reflecting material: heavily doped semiconductor with wide band-gap such as indium tin oxide (In_2O_3:Sn, ITO) and fluorine doped tin oxide (SnO_2:F, FTO) [5]. Compared to metal film, transparent conductive oxides (TCOs) are more transparent and have better chemical and mechanical stability, although the infrared emissivity of these materials is not as low ($\varepsilon > 0.15$) [14, 15]. In the works reviewed [14, 22, 23], thicknesses above 200 nm were used to obtain energy-saving glass films, which is in contrast with the 30–60 nm thickness range commonly used to maximize the transmission around 550 nm for the TCO constituents in D/M/D [24]. In this work, two structures of these kind were fully exploited: GZO/Ag/GZO and GZO/Cu/GZO, which performance was compared with the ITO/Ag/ITO coating previously studied [25]. As it will be shown, best results were obtained from films with a GZO thickness of 20 nm.

The films' microstructure, *i.e.*, the size of crystallite, grain size, grain boundaries, and surface roughness; the thickness and the adjacent materials influence its electrical, optical and emissivity properties [2]. By adjusting these, the D/M/D structure can be adapted to low- or high-solar gain low-e based coating [5]. For example, the ability to reflect IR radiation increases, *i.e.*, ε decreases with increase of the metal thickness. However, due to the predictable decrease in visible transmittance it cannot be continuously increased, with a trade-off between visible transmittance and IR reflectance likely to happen to obtain IR reflection above 80% [5, 6]. Secondly, if the thickness is excessively thin it can lead to photon scattering due to Ag islands formation which can decrease visible transmission and lead to the dips in the spectra [6, 26]. To better understand these results, several authors have investigated the effect of the thickness and adjacent materials on the surface roughness and crystallization [16, 27, 28]. The thickness needed to form a continuous film is dependent on the growth process, undercoat layer and the surface morphology of the substrate. Taking silver as an example, this thickness is around 8-10 nm for sputtered films [5, 16] and $\sim$18 nm for thermally evaporated ones [5]. As for the dielectric, it has been observed that the maximum

transmittance peak shifts to longer wavelengths when increasing top layer thickness [20, 29, 30].

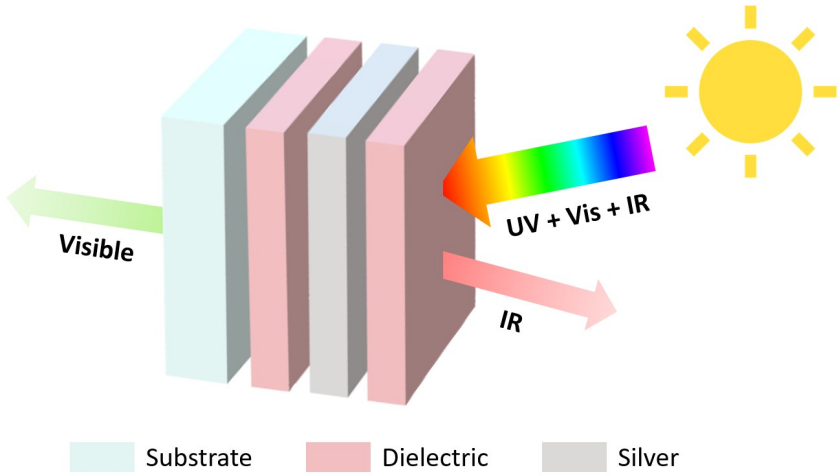

Figure 1.1: Multilayer thin film structure

TCOs must have a wide band-gap of more than 3 eV (transparency in wavelengths above 400 nm) so that more than 80% of visible light can pass through the thin film [24]. Since plasmon absorption wavelength decreases as the carrier concentration increases, doping can lower the IR transmittance. However, when carrier densities exceed $2\times10^{21}\text{cm}^{-3}$ plasmon frequencies shift from absorbing infrared wavelengths to visible light, which reduces the transparency in the visible region [24]. Impurity-doped In_2O_3 , ZnO, and SnO_2 based TCOs are commonly used [24, 31]. FTO is widely utilized to produce low-e hard coatings as it has a high transparency for visible light, high reflectivity for infrared light, high mechanical hardness and good environmental stability [3]. Among these, ITO is the most used TCO material, however, there is a strong need to replace it duo to the scarcity of indium and its toxic nature. Doped ZnO materials, such AZO and GZO have gained importance as non-toxic, cheap and accessible alternatives to ITO [32, 33].

The optical performance can be changed severely by oxidation, agglomeration, interlayer diffusion, recrystallization, delamination, or dewetting. Growth of high quality continuous thin film with few defects is an integral part of IR reflecting coatings [5]. Better thermal stability of silver and enhanced optical properties are obtained if the silver films are successfully adhered to the glass substrates. However, Ag films may have an agglomeration problem, *i.e.*, have island or Volmer–Weber type growth. One way of overcoming this is by introducing an appropriate interlayer between the substrate and Ag film [34] or between the Ag and dielectric metal-oxide layer [13, 35]. Akin Sonmez et al. concluded that, from several metal seeds (Ti, Nb, Cr, Ni, Mo, Pt, Cu, and Ru) of $\sim$1-2 nm in thickness, deposited between Ag and AZO layers, Nb and Ti are more effective than the others in increasing IR reflection of Ag thin films [13]. Doping multivalent metallic elements, such as Cu, Al, Ni, Ti, etc. can also improve Ag thin layer's continuity. As a result, the stability, adhesion and smooth of conductive Ag layer can be economically improved [10, 26]. On the other hand, both transmittance and IR reflectance are impacted in doped films. For example, Zhang et al. observed a decrease in both transmittance and IR reflectance when increasing Al doping concentration of the Ag layer [10].

There are various deposition conditions, multiple arrangements with diverse materials and several deposition methods in high or low temperature or by post annealing to be considered [6]. The film structure depends on the synthesis conditions with the deposition power being a key parameter for the process. The increased plasma power can increase infrared reflection and decrease infrared emissivity due to grain

growth [15]. Similar results were obtained by [14], who also researched the effects of substrate temperature and working pressure. In addition, while residual gas is widely assumed to be detrimental to high-quality metal film deposition, adding proper trace amount of oxygen or nitrogen gas (along with argon gas) during the sputter deposition process can produce ultrathin and continuous Ag or Cu films [26]. Regarding the TCO layers, its deposition conditions play a role in deciding the stability of the metal layer [24]. As previously mentioned, applying a TCO on the metal layer can help prevent oxidation. With that being said, during multilayer deposition, one downside of using oxide materials is associated with the possibility of oxidizing the adjacent ultra-thin metal layers [35]. TCOs' optical properties are highly dependent on oxygen content, e.g., they can lose a portion of their oxygen content and thus transparency in non-reactive physical vapor deposition processes, especially when no oxygen input is used to compensate for oxygen loss. Thus, there are optimums oxygen partial pressures for sputter depositing these layers [24, 35, 36].

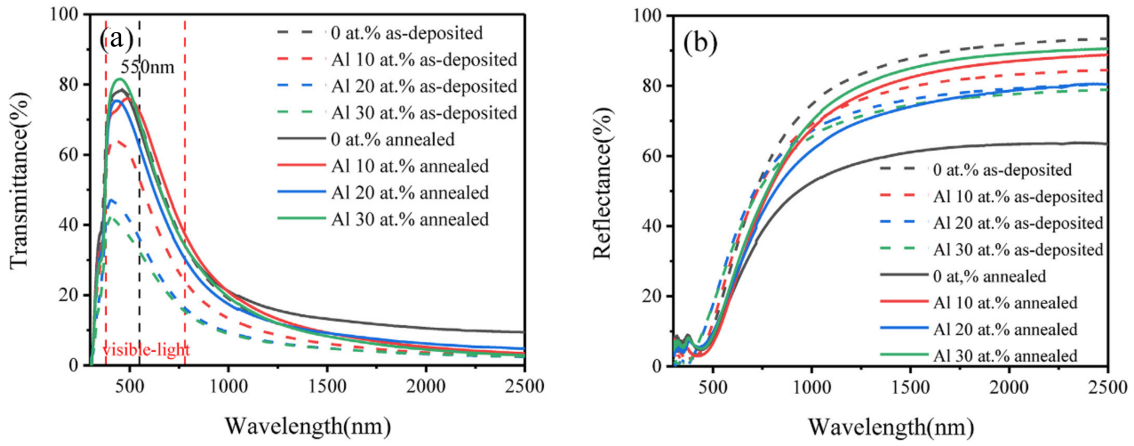

Figure 1.2: (a) Transmittance and (b) Reflectance of ZnO/(Al-doped)Ag/ZnO multilayer films before and after annealing (modified from [10])

The film coated glass needs to be shortly tempered at $\sim$700 °C in coating industry, given that to obtain high quality films thermal treatment is necessary [10]. The visible transmittance usually increases and the absorption decreases following heat treatment due to TCO recrystallization (grain boundaries are responsible for light absorption) [24]. Dalapati et al. observed an 55% to 85% increase in the visible transmittance of TiO_2/Cu/TiO_2 coating and minimal effect in the IR reflection after thermal treatment at 500 °C [11]. At the same time the treatment also can also accelerate the oxidation of Ag, which may ruin the smoothness and continuity of the middle ultrathin Ag layer [10]. However, Zhang et al. demonstrated that by doping the Ag layer with either Cu or Al can effectively suppress O diffusion, preventing Ag from being oxidized and therefore impeding film deterioration and improving low-e performance during thermal annealing. Although Al-doping has been seen to have an adverse effect on the transmittance and reflectance, in all annealed Al-doped films the low-e performance is fully enhanced with the increase of Al-doping concentration (Figure 1.2) [10]. On the other hand, the IR reflectance of ZnO/Ag/ZnO was greatly reduced (from 90% to 60%) after 30 s 680 °C annealing in contrast to Dalapati et al. [11] where oxidation didn't occur until after 500 °C. Additionally, the rapid and selective thermal processing (RSTP) technique can also be used to improve the emissivity of low-e glass in place of increasing the amount of Ag layers in low-e glass. Kim et al. [12] obtained an increase in the SHGC value from 0.39 to 0.42 and a decrease in the ε from 0.064 to 0.053 after RSTP in ultrathin D/M/D multilayers.

1.3 NIR Shielding Nanoparticles

NIR-absorbing nanoparticles (NP) based materials are an alternative route to achieve IR-shielding materials. Examples are: Au-based nanomaterials [37, 38], CuS nanoparticles [39, 40] and WO_3 NPs with ternary additives, namely $C_{sx}WO_3$ [41–43], as they are able to transmit visible light. Besides, to obtain NIR-active properties, a broad variety of anisotropic NIR nanomaterials have been documented, including nanorods, triangles/prisms, nanostars, cubes and nanocages, etc. [44]. That said, solar energy absorbers can also emit heat in the form of thermal IR radiation, from 2.5 μm to 20 μm, which is a significant indirect heat source [45].

When noble metallic nanoparticles (MNPs) such as Ag [46] and Au are stimulated by the incident light, wavelength-selective absorption and scattering can occur due to the resonant oscillation of electrons [47]. This phenomena, the so called surface plasmon resonance (SPR), is sensitive to particle size, shape, and the surrounding dielectric environment [48]. As a result, programmable spectral properties from visible to NIR wavelengths can be generated. The use of plasmonic nanocrystals to make passive IR-blocking glasses is described by Besteiro et al. [49]. Metal oxide nanocrystals are also a compelling path toward tunable plasmonics. In semiconductors, localized SPR (LSPR) can also be programable by varying doping levels and electrochemical potential. For instance, free electron concentrations above 1×10^{21} cm^{-3} have been recorded in ITO nanocrystals, leading to high absorption in the NIR [48]. Transition-metal oxides are interesting candidates as well and Manthiram and Alivisatos [50] demonstrated that with metallic phases of $WO_{3-\delta}$ nanoparticles.

NIR region absorption resulting from energy band transitions instead of surface plasmon resonance is an alternative. Multiple kinds of narrow band gap metal chalcogenides, such as PbS, PbSe, PbTe, CdTe, HgTe, ZnS, CdS, and PbS are used in infrared detection applications or have been researched intensively [39, 51, 52]. However, the toxicity of these nanoparticles is an issue for certain applications. Attractively, copper sulfide (CuS) and silver sulfide (Ag_2S) have the advantages of suitable bandgap, low toxicity, and high absorbance coefficient, although CuS nano-crystals have been shown to exhibit high NIR absorption due to their LSPR [39, 52, 53]. CuS being a cost-effective material composed of abundant earth elements, it is an ideal substitute for $C_{sx}WO_3$, noble metals, ITO, antimony-doped tin oxide (ATO) and gold for solar shielding and photothermal applications. Therefore, this was also one of the materials that in this thesis was selected to try to improve NIR blocking ability. Rokade, Jin, and Park using 1 wt% CuS thin film managed to shield moderately NIR radiation (800-1400 nm), even though the visible light transmittance was of $\sim$40-50%, reducing even more with increase of NPs quantity. Furthermore, CuS and CuS/PVA thin films transmittance spectra were clearly different with the latter exhibiting superior solar-shielding ability [39]. As for Ag_2S nanomaterials, also used in this thesis, which have shown to possess strong absorption in both NIR light (up to $\sim$1200 nm from my view point) and visible light regions [52, 54]. Ag_2S is a direct narrow-band gap semiconductor, of $\sim$ 0.9-1.05 eV corresponding to the photon energy in the NIR range [52]. Besides the already mentioned sulfide NPs, tin sulfide has also received considerable attention. It has a variety of phases, each possessing different bandgap energies like 1.3 eV (SnS), 2.18 eV (SnS_2S) and 0.95 eV (Sn_2S_3) [55]. SnS holds strong absorption properties, yet dissimilar direct bandgaps for NPs and films, fluctuating between 1.3 and 1.92 eV, a blue shift attributable to quantum effects [55–57].

2 Materials and Methods

2.1 Deposition of Metallic and Oxides Thin Films

The GZO films were deposited by radio frequency (RF) magnetron sputtering (*Mantis*). The films were deposited onto 100×100×1 mm^3 Borosilicate float *MarienFeld glass* substrates or in smaller coated ones (*e.g.*, 2.5×2.5 cm^2). This substrate size was glued to a bigger glass with Kapton tape and placed in the target position of the vacuum chamber.

GZO targets, ZnO:Ga_2O_3 (95:5 wt%), were supplied by Super Conductor Materials Inc with purity of 99.99%. The deposition was performed at 13.6 sccm Ar gas flow and depending on the different powers used, the pressure ranged between 7×10^{-4} and 2×10^{-3} mbar.

The deposition of the metallic layers, Cu and Ag, and of the electrodes, Al, was done by resistive thermal evaporation of metallic pellets (*Super Conductor Materials, Inc.*) with 99.99% purity in a tungsten boat. The pressure inside the thermal evaporation chamber was maintained around 10^{-6} mbar (by using a turbo molecular pump in conjunction with a rotary pump) and the thicknesses were set to be around 5 nm, 11 nm and above 120 nm for Cu, Ag and Al, respectively. Hence, sputtering and thermal evaporation techniques were alternately used for preparing the TCO/Metal/TCO coatings. Annealing of copper multilayers was done using a tube furnace OTF-1200X connected to a turbo Pfeiffer Vacuum pump (HiPace 80) at a pressure of $\sim10^{-5}$ mbar and under a controlled nitrogen atmosphere.

2.2 Synthesis and Deposition of Ag_2S and CuS Nanoparticles

2.2.1 Synthesis

Ag_2S was synthetized using two alternative approaches, microwave (MW) assisted synthesis and ultrasonic irradiation (UI), a sonochemical method. The CuS was only obtained by the microwave-assisted process. Copper (II) oxide (CuO, Alfa Aesar, 99.0% min) and 1-dodecanethiol (DDT, *ALDRICH*, $\geq$98.0%) were utilized as the precursors of CuS, and Ag_2S MW nanoparticles were prepared from silver nitrate ($AgNO_3$, *SIGMA-ALDRICH*, $\geq$99.8%) precursor. The procedure is described in a previous work [58], using a microwave (*Monowave 400*). After synthesis, the MW nanoparticles were dried using the vacuum drying method. For the synthesis of Ag_2S nanoparticles prepared via ultrasonic irradiation (Ag_2S UI), the same precursor was used, 0.2888 g of $AgNO_3$ was added to 10 mL of DDT to reproduce the work described by Kang et al. [59]. After the drying process (in an oven at 80 °C), the material was ground into powder.

2.2.2 Deposition

The nanoparticles were deposited by electrospray (ES). The setup used is shown in Appendix B. The conductive GZO coated glasses of $\sim$2.5×2.5 cm^2 were mounted on the target, a bigger glass of 100×100 mm^2 glass covered with aluminum foil. Electrostatic focusing of the electrosprayed nanoparticles pumped through the needle at a flow rate (μL/h) was made by placing a ring between the needle tip and the target. The needle and the ring electrode were connected to the positive electrode of a DC power source. Additionally, a tape of aluminum foil strap was also used to make the electrical grounding connection. The distances needle-tip/ring and ring/target were adjusted to 4 cm and 8 cm, respectively.

The solution where the nanoparticles were in suspension was prepared as follows: x mg of nanoparticles were added to 1 mL ethanol (*Honeywell Riedel-de Haë*, $\geq$99.8%) to achieve the concentration of x=1,2,4 mg/mL. Next it was transferred to a syringe placed into a syringe pump (New Era Pump Systems,

Inc.) that delivered the NPs solution at a volume flow rate of 980 µL/h. Before introducing the dispersion in the syringe, it was sonicated for 3-4 minutes to deagglomerate the NPs. In the Ag_2S UI case, it was needed a longer sonication time (30 min) for dispersing the nanoparticles. Because some of the solvent evaporated during the process, ethanol was added to fill up to 1 mL (the initial level had been marked).

The applied voltage was 19 kV and experiments were performed in ambient temperature while monitoring temperature and humidity level. If humidity was high, a small heater was turned on to make it drop to a constant level (around 37%), *i.e.* beneficial to films deposition and in particular to solvent evaporation during the process.

2.3 Characterization

The films and coatings optical properties were studied by using UV Vis-NIR Spectrophotometer *Jasco V-770* in the wave-length range of 200-2500 nm using an integrating sphere. The absorption spectrum (A) was obtained from the transmittance (T) and reflectance (R) through equation: $A(\%) = 100–T(\%)–R(\%)$.

Characterization of the nanoparticles surface morphology was performed with a Hitachi S2400 Scanning Electron Microscope (SEM) operated in Secondary Electron Imaging (SEI) mode and a JEOL 7001F at IST and with a WITec Alpha 300 RAS the Atomic Force Microscope (AFM).

X-ray crystallography analysis was performed in an X-ray diffractometer (XRD) PANalytical X'Pert PRO equipped with an X'Celerator detector using Cu K_α radiation (1.540598 Å) at 45 kV and 40 mA, in a Bragg–Brentano configuration. The XRD diffractograms were collected over the angular 2θ range of 10-90° with a scanning step of 0.03°. Besides crystal structure, XRD also allowed to identify the crystal phases present in the metallic sandwich structures, and thus, also revealed chemical composition information. Phases identification made through comparison of the acquired data to that in referenced databases. Chalcogenide nanoparticles composition was analyzed via Raman spectroscopy on a Witec Alpha 300 confocal RAS with a 532 nm Argon Laser at 2.5 mW of power. The exposure time for all spectra was of 500 s.

The metallic and oxide coatings compositions and thicknesses were determined by Particle Induced X-ray Emission (PIXE) and Rutherford Backscattering Spectrometry (RBS), with experimental set-ups and analytical possibilities extensively described in the literature [60]. These tests were carried out on the LATR 2.5 MV Van de Graaff accelerator at CTN/IST. PIXE elemental analysis enabled checking the films for unwanted contamination (down to ppm levels). PIXE spectra evaluation was done with the GUPIX code [61].

Electric and thermoelectric characterizations were performed with a home-made setup [62], that allows applying a thermal gradient (ΔT) in the plane of the samples by measure of two *TEC1–12707* Peltier modules, supplied by two independent power sources, and measuring a thermoelectric voltage (ΔV) with an *Agilent 34420 A* nano-voltmeter, which also enables resistance measurement at the in-plane Al electrodes (with an area of 3 × 6mm^2, 3 mm separated and 120 nm thick) deposited on top of the GZO film. Seebeck coefficient was obtained from the slope of the plot ΔV vs. ΔT, where this was monitored and measure by a *FLIRA310* thermal camera.

The efficiency of the coatings was demonstrated by comparing the temperature inside a closed cubic box with a glass face irradiated by a Halo Go standard lamp of 20 W to simulate the effect of the sun. Inside the box a temperature sensor was connected to a computer-controlled Data-Logger (*Keysight 34972A*) for monitoring the temperature over time for 60 min (step 1 min) and compare with that outside the box (monitored by another temperature sensor) which enabled to plot Temperature vs. Time curves.

3 Results and Discussion

3.1 Metal-Oxide Coatings

This section deals with oxide and oxide-metal films. First, a study focusing on the optimization of the GZO deposition parameters to show the effect of time and rf power on thickness and roughness and optical properties of the films. After selecting the optimal sputtering parameters, *i.e.*, the optimal thicknesses of the low-e coatings, GZO films, two metallic coatings were tested, Ag and Cu. The optical performance of both types of GZO-metallic coatings was compared with that of an ITO/Ag/ITO coating previously optimized. All produced coatings were characterized by a number of techniques for accessing their properties *e.g.*, composition, structural, electrical and emissivity properties.

3.1.1 GZO Films - Thickness Optimization

Following the preliminary results in appendix A, the effect of sputtering power and deposition time on the GZO films thickness, surface morphology and roughness as well as in their optical properties was investigated with GZO/Ag/GZO (as silver can withstand higher sputtering power) and after optimization the GZO/Cu/GZO coating was repeated (results are shown in section 3.1.2).

The study was performed in two ways: first, the power was varied from 50 W to 200 W while keeping all the other deposition parameters unchanged, including the deposition time set to 1 h, and second, the power was set to 200 W while the sputtering time was adjusted to 0.5 h, 1 h and to 2 h.

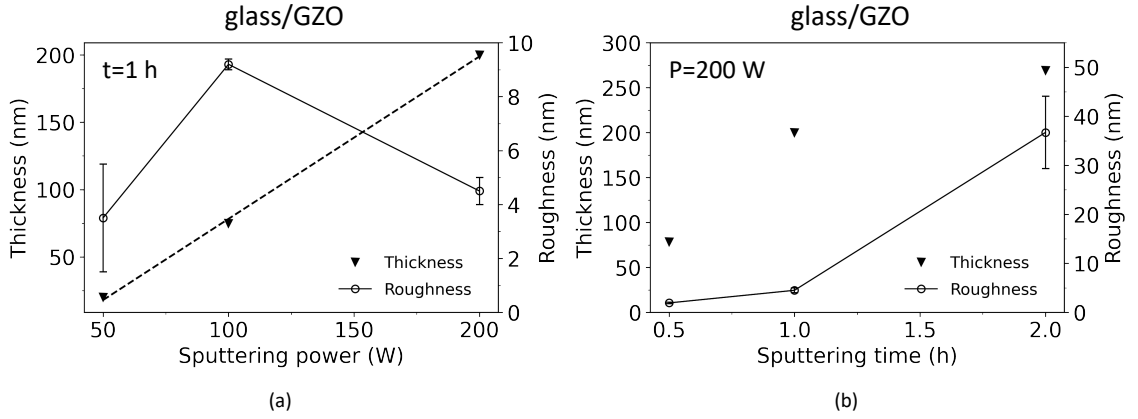

Figure 3.1: Effect of (a) sputtering power with time set to 1 h and (b) time on thickness and roughness with power set to 200 W

Sputtering power has a significant impact on both the deposition rate and the thickness of the films [63]. With the deposition time fixed to 1 h and the power, 50W, GZO film thickness was measured to be ∼20 nm. Due to the deposition rate increase, the thickness of the films deposited at 100 and 200 W was 75 and 200 nm, respectively. From the Figure 3.1(a) it is observed that the film thickness linearly increased with power. RBS spectra from where thickness was extracted are shown in appendix C with a table summarizing sputtering conditions and corresponding thicknesses. The mean roughness was also calculated together with the standard error ($SE = \sigma/\sqrt{n}$). At the sputtering power of 100 W, the roughness was the highest, with 9.2 nm. A power of 50 W, on the other hand, resulted in a lower mean roughness, however it has a greater variability in the roughness values measured at distinct points throughout the surface. Between

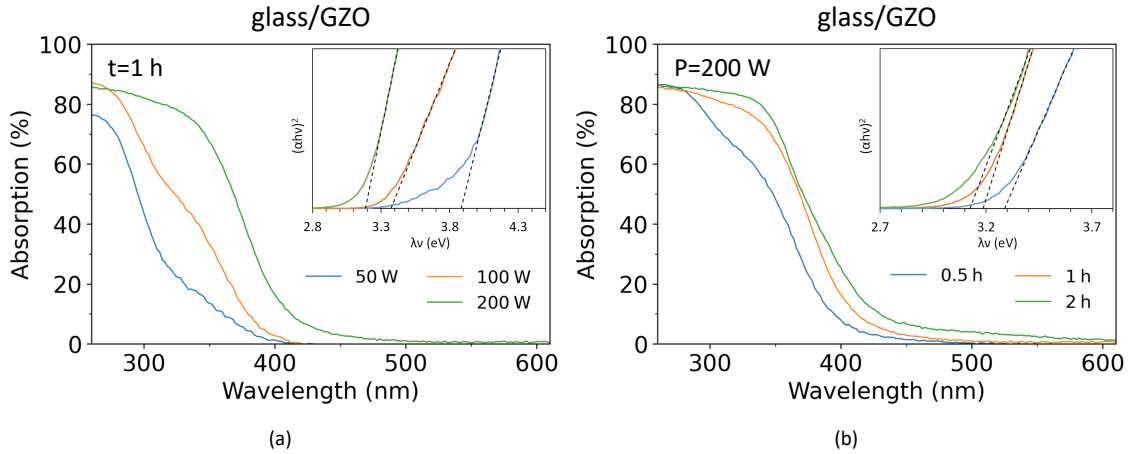

Figure 3.2: Effect of (a) sputtering power with time set to 1 h and (b) time with power set to 200 W on band gap

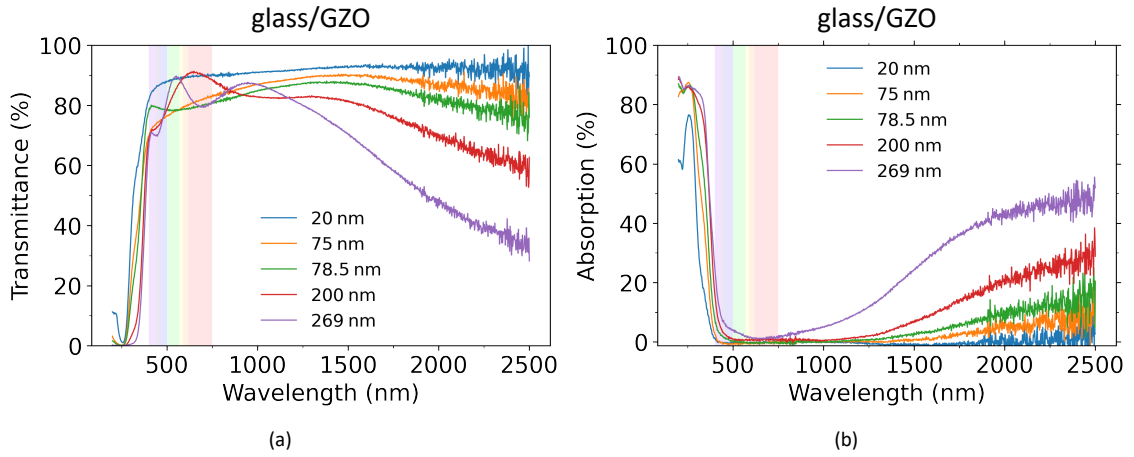

Figure 3.3: (a) Transmittance and (b) Absorption spectra of GZO films with thicknesses varying from 20 to 269 nm

the 50 W and 100 W, increased power resulted in a transmittance drop, which could be attributable to increase of surface roughness which promoted the light scattering and reflection [63].

Figure 3.1(b) shows how the GZO films thickness and roughness of GZO film varies as a function of sputtering time with the power set to 200 W. It can be observed that as expected, the thickness of GZO thin film increases with sputtering time. The roughness is also increased with the deposition time. At the sputtering of 0.5 h the surface was the smoothest (1.9 nm). A 2-hour deposition gives a high mean surface roughness (36.7 nm) and high variability (7.3 nm). A big difference in surface roughness can be observed between both samples, maps are shown in appendix C. In general, the high roughness and the high light transmission due to the strong light scattering are a pair of competitive characteristics [64]. Interestingly, it can be shown that the GZO 2h 200 W (GZO200) coated glass has a better visible transmittance compared with GZO 0.5 h. The interference phenomena allowed for greater visible transmission.

The start of band gap absorption causes the transmission to drop significantly in the UV-Vis band. Figure 3.2 shows this phenomenon for GZO films deposited at different sputtering conditions. It's worth noting the red shift of the absorption edge indicates a continuous reduction of optical band gap of films as the power and time increase. Actually, it was observed that the band gap decreases as the film thickness

increases. According to [65], Burstein–Moss shift is responsible for this change in band gap. The band gap absorption edge for ZnO is in the ultraviolet range, however as carrier density increases, it may shift to shorter wavelengths.

As for the observed NIR drop increased with the sputtering power and time, *i.e.*, with the increasing film thickness, it can be attributed to the plasmonic resonance with wavelength around 2500 nm. Films with even greater thicknesses than the ∼270 nm should be better for IR-blocking glasses, but it is not known how the visible spectra would be affected. Zhu et al. [66] worked with ∼500 nm GZO films with good average transmittance.

3.1.2 GZO-Metal Structures

The transmittance spectra of GZO/Ag/GZO coating as a function of the rf power for the GZO films is shown in Figure 3.4. A shift of the maximum transmittance to longer wavelengths with the introduction of the GZO layer is observed as well as an increase of its thickness up to 75 nm (100 W) [29]. Additionally, the peak height and width are greater which lead an increase in the coating's transparency. The GZO 200 nm thick (1 h 200 W), which caused a decrease in Tvis, is too thick for the aimed application. The 20 nm to 75 nm thicknesses range of that typically used for TCO/Metal/TCO coatings [24, 29].

The optimal thickness for the GZO layers in the low-e structure was determined to be 20 nm (50 W 1 h - GZO50) because of its higher T in visible range and higher IR reflectivity in the 1000s nm wavelengths where the solar radiation is more intense. At the same time, by comparing this GZO composed film with the optimal ITO/Ag/ITO coating obtained in a previous study (results in Table 3.1), it's shown that they present comparable NIR reflecting properties [25]. The maximum transmittances of these two structures are similar, however it can be seen that the ITO structure presents a peak more centered in the visible, that is, closer to 550 nm (wavelength the human eye is most sensitive to). To improve the structure, a study on the effect of GZO thickness between 20 nm and 75 nm may be beneficial, if it follows the trend the peak will shift to the right with thickness increase.

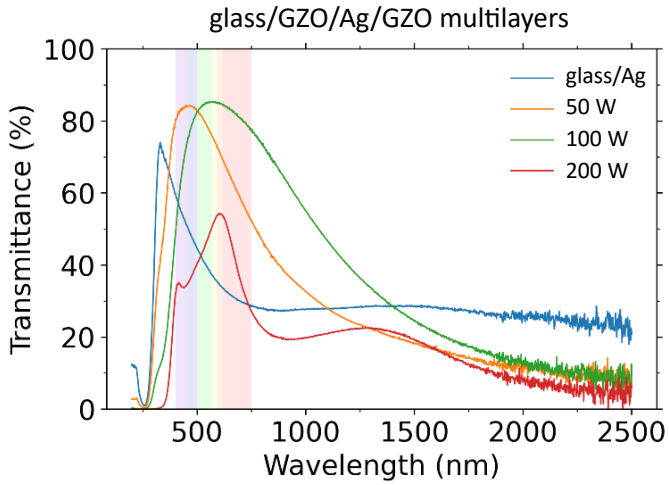

Figure 3.4: Transmittance of Ag multilayer thin film structures, namely glass/Ag and glass/GZO/Ag/GZO for 3 different GZO thicknesses

Different multilayers structures were produced with the 20 nm GZO films and 5 nm thick Cu and 11 nm Ag layers. In figure 3.5 it is shown that the transmittance significantly increases in the visible when the GZO top layer is added to the glass/GZO/Ag bilayer structure. Thus, the top GZO layer appears to act as

anti-reflective film (as reported in the literature and required by low-emission coatings for glass windows applications) and contributes to prevent the metallic layer oxidation. In the infrared region of the spectra, the introduction of a GZO layer between the glass and the metal, improved the IR blocking due to an enhancement in the reflectance as shown in Figures 3.5(b) and 3.6(b).

As already indicated, thicker GZO films (higher than 269 nm) have the potential to constitute IR shields. For the case at hand, coatings 45 nm (Cu structure) and 51 nm (Ag structure) thick were obtained. The advantage of tri-layer is that the desired optical properties can be achieved with a significantly smaller thickness.

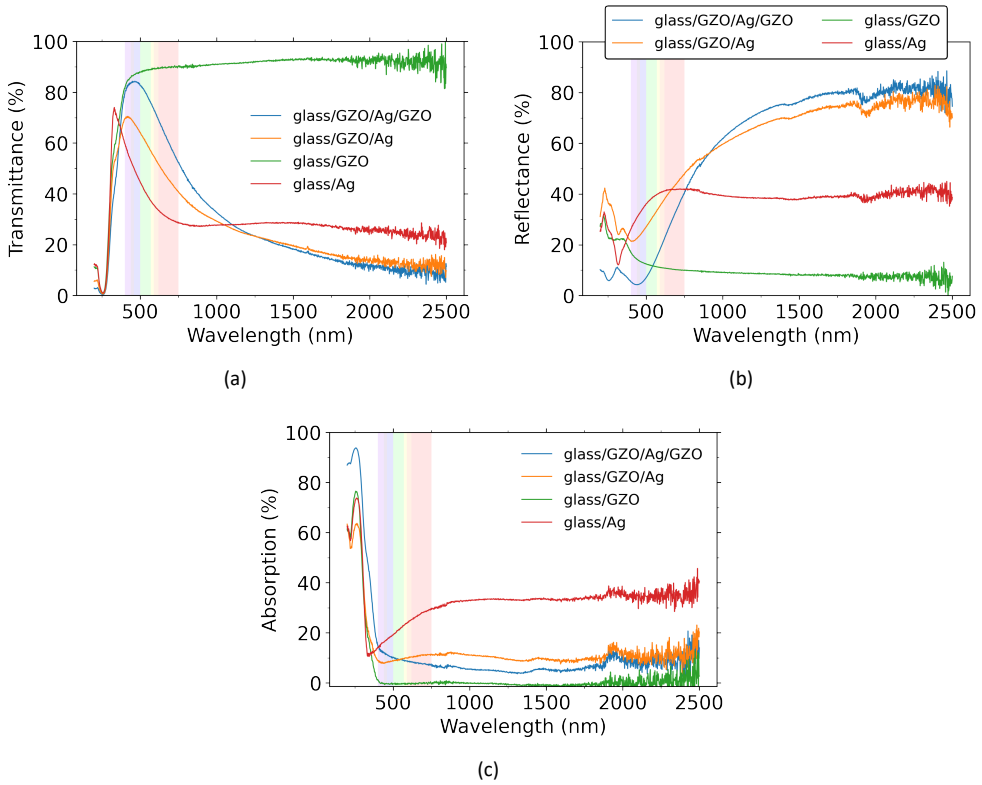

Figure 3.5: (a) Transmittance, (b) Reflectance and (c) Absorption spectra of GZO with deposited silver layers

In the visible wavelength range, the transmission spectra are influenced by the absorption of light in the Cu thin layer due to the electronic transitions between the bands, in particular due to the excitation of electrons from the d band to the Fermi surface [11].

The results showed that silver allows one to have a higher reflectance in the NIR and is simultaneously more transparent than copper. The GZO (20 nm)/Metal/GZO (20nm) multilayers obtained a transmittance at 550 nm of about 78.1% and 63.1% and a NIR reflection of 80.1% and 72.7% for the Ag and Cu, respectively. In Table 3.1, the obtained properties are compared with those of other D/M/D films in literature. For the copper structure to reach the same level of IR blocking, one would have to, for example, increase the thickness of the metal. However, this would theoretically decrease the transmittance even more. Since copper is a transition metal with a high optical absorption of visible light, GZO/Cu/GZO has a low overall optical transmittance [11, 67]. On the other hand, it might be possible to increase the transparency of the film in the visible, through the annealing of the Cu layer and oxide structure [67–69]. Therefore, the GZO/Cu/GZO samples were annealed in vacuum in the following conditions: 400 °C for 45 min, 500 °C for

45 min, 400 °C for 90 min. These time values were chosen to investigate the effect of temperature and annealing time on the optical properties of the GZO/Cu/GZO. Results are shown in the next sector.

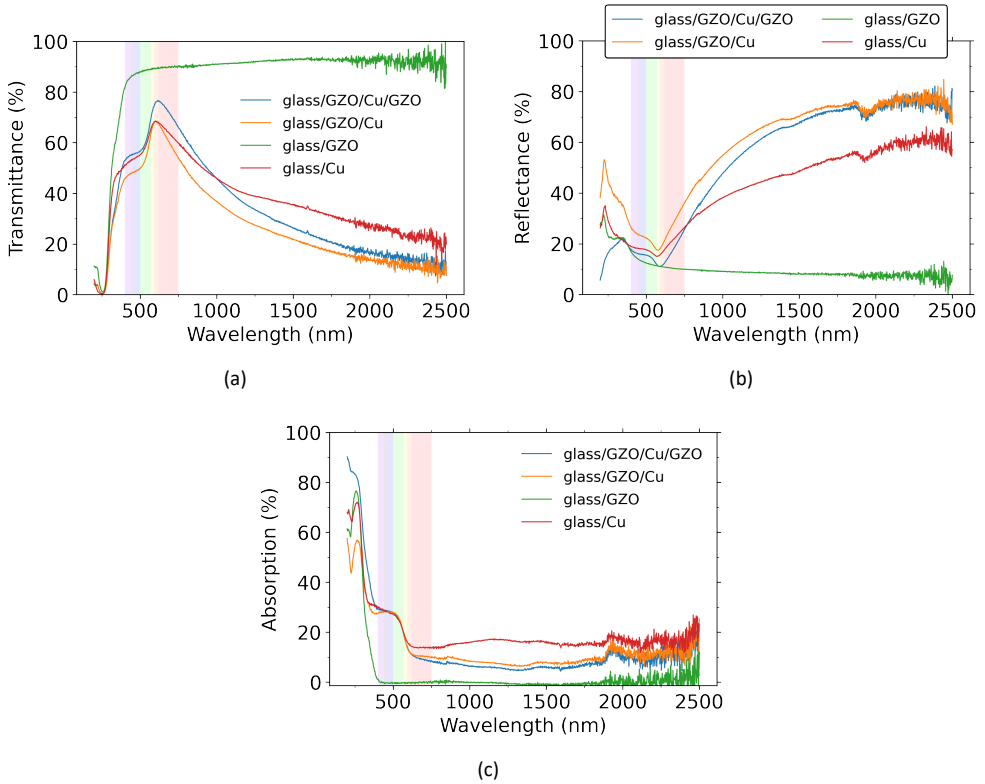

Figure 3.6: (a) Transmittance, (b) Reflectance and (c) Absorption spectra of GZO with deposited copper layers

3.1.2.1 Annealing of GZO-Cu Structures

Figure 3.7 shows the optical spectra, transmittance, reflectance and absorption spectra, measured before (as grown curve) and after performing each type of annealing (temperature and duration). A decrease of the film's visible transmittance from ∼595 nm on is visible and at this wavelength there is a peak that becomes more pronounced after annealing. It is the result of increased reflectance and mostly absorption. The wide broad light absorption in the near IR can be related to the local surface plasmon resonance and light scattering. The IR blocking ended up increasing as well because of this effect and annealing is helpful in this regard. The temperature 500 °C had the greatest effect on film absorption. Therefore, in a future work, higher annealing temperature may be considered and for the optimal temperature a longer annealing should be tried.

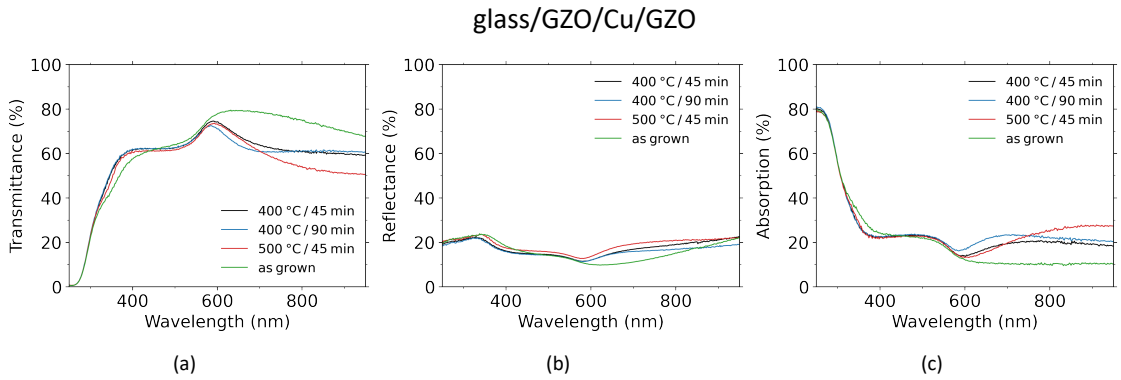

Figure 3.7: (a) Transmittance, (b) Reflectance and (c) Absorption spectra of annealed GZO50/Cu/GZO50

Table 3.1: The optical properties of samples from this work and other researches. T_{ave} and R_{ave} are the average visible transmittance and NIR reflectance, respectively.

Structure	Visible Transmittance	NIR Reflectance	Reference
GZO(20 nm)/Ag(11 nm)/GZO(20 nm)	$T_{\lambda=550\ nm} = 78.1\%$	$R_{\lambda=1900\ nm} = 80.1\%$	This work
GZO(20 nm)/Cu(5 nm)/GZO(20 nm)	$T_{\lambda=550\ nm} = 63.1\%$	$R_{\lambda=1900\ nm} = 72.7\%$	This work
ITO(40 nm)/Ag(20 nm)/ITO(40 nm)	$T_{ave} = 80\%$ $T_{\lambda=550\ nm} \sim 85\%$	$R_{\lambda>1100\ nm} = 80\%$	[25]
ZnO/Ag/ZnO (total thickness: 33.8 nm)	$T_{ave} = 74.2\%$ $T_{\lambda=550\ nm} \sim 81\%$	$R_{ave} = 62.8\%$ $R_{\lambda=1900\ nm} \sim 77\%$	[6]
V_2O_5(20 nm)/Ag(10 nm)/V_2O_5(20 nm) annealed at 550 °C for 30 min	$T_{\lambda=500\ nm} = 71\%$	$R_{\lambda=1100\ nm} = 81.9\%$	[20]
TiO_2(48 nm)/Ag(18 nm)/TiO_2(48 nm)	$T_{ave} = 62.5\%$ $T_{\lambda=550\ nm} \sim 73\%$	$R_{ave} = 71.9\%$ $R_{\lambda=1900\ nm} \sim 90\%$	[11]
TiO_2(50 nm)/Cu(20 nm)/TiO_2(50 nm)	$T_{ave} = 59.8\%$ $T_{\lambda=550\ nm} \sim 57\%$	$R_{ave} = 85.6\%$ $R_{\lambda=1900\ nm} \sim 93\%$	[11]

3.1.2.2 Composition, Structural and Electrical characterization

3.1.2.2.1 PIXE and XRD

PIXE elemental analysis enabled checking the films for unwanted contamination (down to ppm levels). The composition is consistent with the nominal compositions indicated by the supplier for GZO target and no contaminants were detected in the films: the PIXE spectra in Figure 3.8 only show the elements Ga and Zn from the GZO and Ag and Cu from the metal layers, along with elements from the glass substrate (*e.g.*, Si, Ca and Sn), no other elements were detected. The Sn are present in the borosilicate glass as it was grown by a float process making use of a tin bath [70].

To further study the structural properties of the GZO/Ag/Cu and GZO/Cu/GZO coatings, the XRD patterns were investigated, as shown in Fig 3.9. It is observed that all the films are polycrystalline.

The broad peaks at 24° are due to the glass substrates. The common peaks around 33.5° are close to that of the standard ZnO crystal (34.45°). It means the presence of a hexagonal wurtzite structured

GZO with a preferential orientation in the (002) plane [71] which means the c-axis is perpendicular to the surface of the substrate.

The diffraction peak of silver corresponding to the (111) plane was observed at $\sim$ 38.1° [13, 28]. The peak at 43.4° is assigned to the Cu (111) [72]. The low intensity peak of Cu may be related to its low thickness (5 nm).

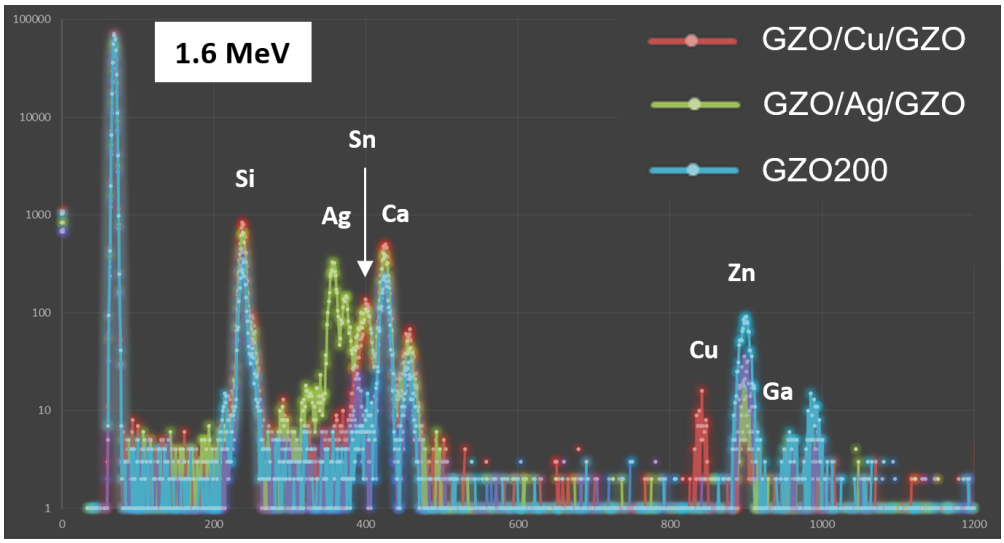

Figure 3.8: PIXE results of Ag and Cu trilayers

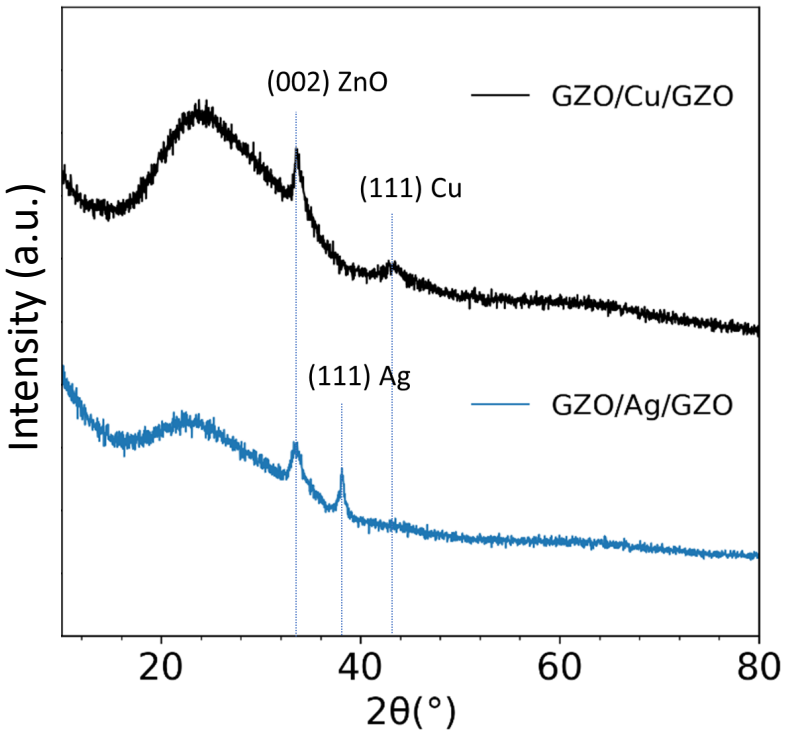

Figure 3.9: DRX pattern of Ag and Cu trilayers

3.1.2.2.2 Thermoelectric Properties

The thermoelectric properties of the GZO/metal/GZO coatings, *i.e*, with a metallic layer of Ag or Cu were measured in planar configuration as previously explained (figure 3.10). The voltage measured as a function of the temperature difference applied to each sample was obtained. From the linear fit of each curve was possible to extract the Seebeck coefficient (which is the slope of those lines, *i.e*, ΔV/ΔT) and the results are presented in Table 3.2. This also includes electrical properties such as the resistivity derived from the measured resistance. One can conclude that the Seebeck coefficients are very small and not very competitive with other materials used in thermoelectric applications (*e.g.*, photothermoelectrics), and the resistivity values are one order of magnitude higher for this kind of structure [18]. The values were calculated from equation 3.2, relating resistance with resistivity.

$$S = \frac{K_s}{e}\left[-\frac{\Delta E}{K_s T} - \frac{3}{2}\right] \tag{3.1}$$

$$\rho = R\frac{w \times t}{l} \tag{3.2}$$

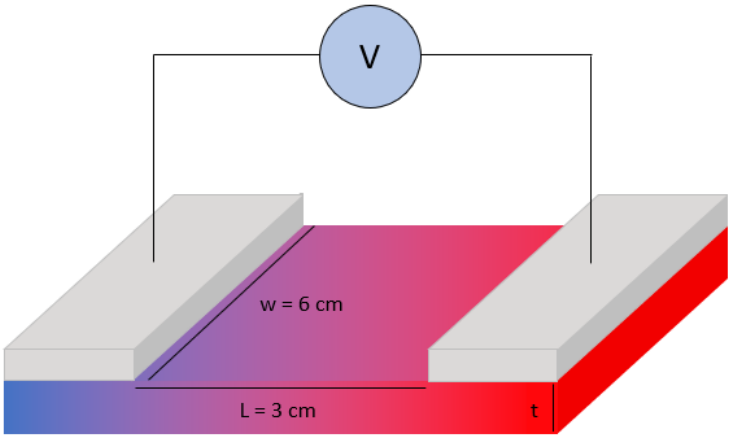

Figure 3.10: Seebeck effect

Table 3.2: Thermoelectrical and electrical properties of samples

	GZO/Ag/GZO	GZO/Cu/GZO
S (μV/K)	- 7.20	- 8.11
ΔE (meV)	- 36.4	- 36.13
Resistivity (mΩ.cm)	0.33	0.14

3.1.2.3 Temperature Effect of Films

The films produced were tested in a closed box with incidence of light to understand if their optical transmittance, reflectance, or absorption were suitable to control the temperature inside box due to infrared light reflection, or absorption. The films chosen for that test were the the GZO (20 nm) which lets IR pass through and the NIR shielding ones such as GZO (20 nm)/Ag, Cu/GZO (20 nm) and GZO (75 nm)/Ag/GZO (75 nm). The uncoated glass was used as a reference. The optical properties are listed in Table 3.3.

Figure 3.11 depicts a graph of the temperature as a function of time. The film that produced the lowest temperature rise was GZO20 nm/Ag/GZO20 nm, which is in accordance with the optical properties shown. Besides, the temperature difference between the film and the uncoated glass (glass) was of 9.4 °C, which corresponds to a temperature drop of approximately 20%. It is also observed a considerable temperature decrease in the remaining films that present infrared blocking. Therefore, the obtained low-e films were considered efficient.

This turned out to be a method with low reliability when the results varied depending on the day and time of day the test was taken.

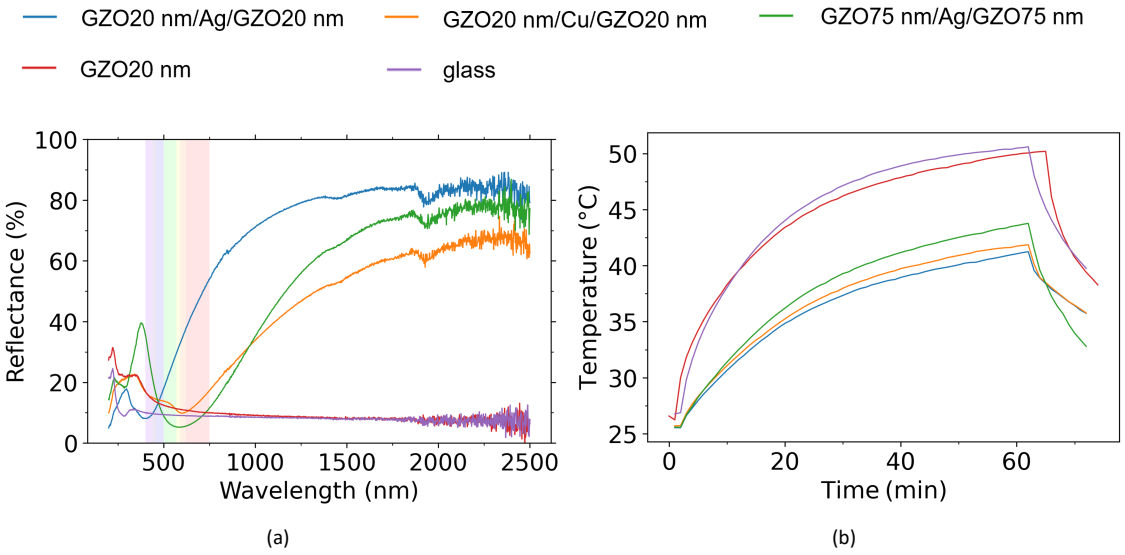

Figure 3.11: (a) Reflectance spectrum and respective (b) temperature versus time graph of studied films

Table 3.3: Optical properties of samples

Structure	Transmittance at 550 nm (%)	Reflectance at 1900 nm (%)
GZO 20 nm/Ag/GZO 20 nm*	68.6	82.3
GZO 20 nm /Cu/GZO 20 nm*	66.6	60.5
GZO 75 nm/Ag/GZO 75 nm	85.0	74.3
GZO 20 nm	88.7	7.9
glass	91.2	7.4

* The GZO 20 nm/Metal/GZO 20 nm structures present slightly different optical values from the ones mentioned previously as they belong to a different batch.

3.2 Synthesis and Deposition of Ag_2S and CuS Nanoparticles

The silver sulfide nanoparticles were obtained by two alternative approaches: sonochemical (UI) and microwaved assisted methods, while the copper sulfide was obtained just by the latter one. Micro Raman spectroscopy was performed to analyze the nanoparticles chemical composition and SEM for accessing the morphology. Next, Ag_2S by UI were used to perform a systematic electrospray study aiming to determine the optimal deposition parameters to get the most uniform NPs distribution on the target substrate (GZO on glass) and the desired absorption spectrum. In addition, XRD analysis was also performed on the nanoparticle films.

The sonochemical method had the advantage of allowing the production of a larger quantity of NPS than the microwave assisted one. On the other hand, microwave preparation provides excellent control of experimental parameters and higher reproducibility.

3.2.1 Characterization

3.2.1.1 RAMAN

The spectra shown in Figure 3.12 were acquired with a very low power of 0.2 mW and optimal measuring time for avoiding heating the samples and having related effects in the spectra. Moreover, because Ag_2S is known to be highly photosensitive [73]. The 532 nm laser was selected as the exciting source. All measured spectra in exhibit low intensity and have broad peaks, which may denounce crystalline lattice disorder of the nanoparticles. Ag_2S spectra obtained by both spectra are similar and the main Raman modes appear in the frequency region 50-134 cm^{-1} and at the broadened band centered around 230 cm^{-1}. According to the literature, the modes at the lower wavelengths may be assigned to A_g and B_g vibrational modes and that, the one corresponding to the Raman peak at 230 cm^{-1} is a combination of asymmetric stretching and bending Ag-S-Ag A_g mode. But, comparing the position of this mode peak in the figure with that of the literature, a small 10 cm^{-1} shift was detected to the left, which may be related with the different size of the NPs in analysis and/or with any lattice deformation effect. A_g modes are reported to be a combination of asymmetric stretching and bending modes of Ag-S-Ag bonds and B_g are mainly described as bending modes. The detected vibrational modes match with that reported for monoclinic crystal structure called β-Ag_2S (with the mineral name acanthite). Result that it was not possible to confirm with XRD data, since XRD analyzed Ag_2S nanoparticles were deposited on top of a GZO film, which signal was the most prominent.

The two most prominent Raman peaks that are typical of CuS single crystal are reported to be at $\sim$474 cm^{-1} and 265 cm^{-1}. Usually, the first one is more intense and due to the S-S stretching mode of S^{2-} ions [74]. However, the Raman spectrum obtained for the CuS nanoparticles shows two broad peaks centered at $\sim$92 cm^{-1} and $\sim$290 cm^{-1} which are possibly assigned to Cu_2O and CuO but not to CuS. The fact that any signal was detected from CuS characteristic bands probably means that CuS amorphous nanoparticles were synthetized [75], but this could not be confirmed by XRD because CuS nanoparticles were on top of GZO, which was again the predominant signal. On top of that, the optical properties of the obtained NPs, which are presented in section 3.2.3, are more similar to that of CuS [76, 77]

According to the literature, the broad Raman peak at $\sim$92 cm^{-1} has a long tale at the right side that may result from the combination of 108 cm^{-1}, 146 cm^{-1} and 218 cm^{-1} modes of Cu_2O. The other peak at $\sim$290 cm^{-1} should correspond to the CuO A_g modes [78]. Finding these phases in the 'CuS nanoparticles' is not completely surprising because CuO is the precursor and the reaction may for some reason have not

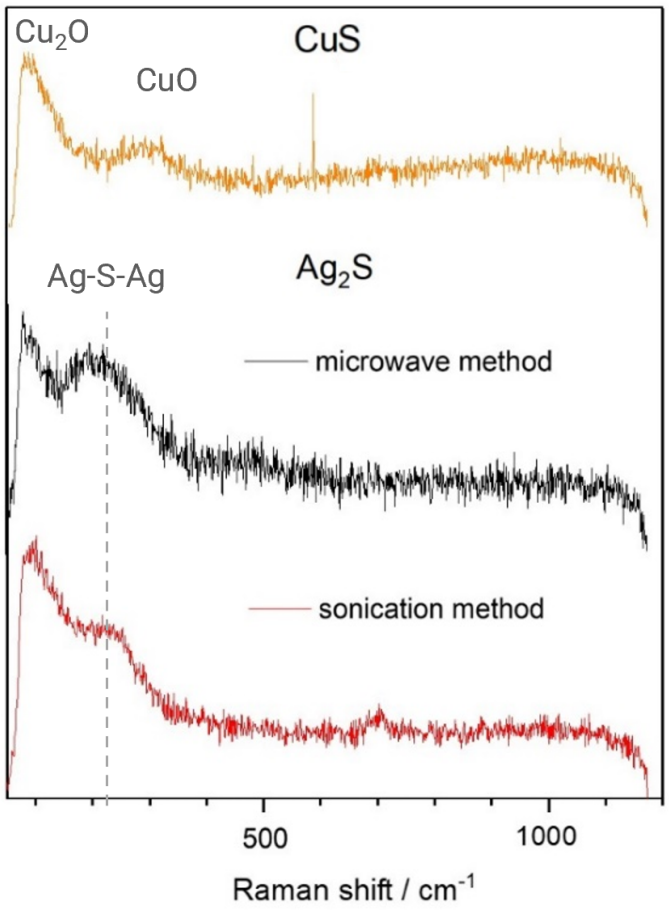

Figure 3.12: RAMAN spectrum of sulfide nanoparticles

occurred completely, and it is not to exclude that after few days other CuO oxides as Cu_2O may have formed too.

Also note, that one Raman spectrum was shown per sample, but that more than one spectrum was taken per sample and all were similar, nevertheless the analyzed points maybe not representative of the entire sample. Further composition characterization of these synthetized nanoparticles is required.

3.2.1.2 SEM

As clearly shown in SEM images (Figure 3.13), there is agglomeration/aggregation of Ag_2S and CuS nanoparticles. As a result, estimating the true particle size is a challenge.

The nanoparticles produced by ultrasonic irradiation had to be sonicated during 30 min or more to be able to disperse in the ethanol. Figures 3.13(c) and 3.13(d) show the SEM images before and after sonication. Prior to sonication, the aggregates reached a size greater than 100 µm. Compared with the nanoparticles obtained by microwaved process there is a very significant disparity in size. This can be explained by the drying process that takes place after washing. While MW nanoparticles procedure involved a method of vacuum drying, the Ag_2S US were dried in an oven at 80 °C which promoted the aggregation. In fact, because the image refers to the powder obtained after grinding, the aggregation size was even greater.

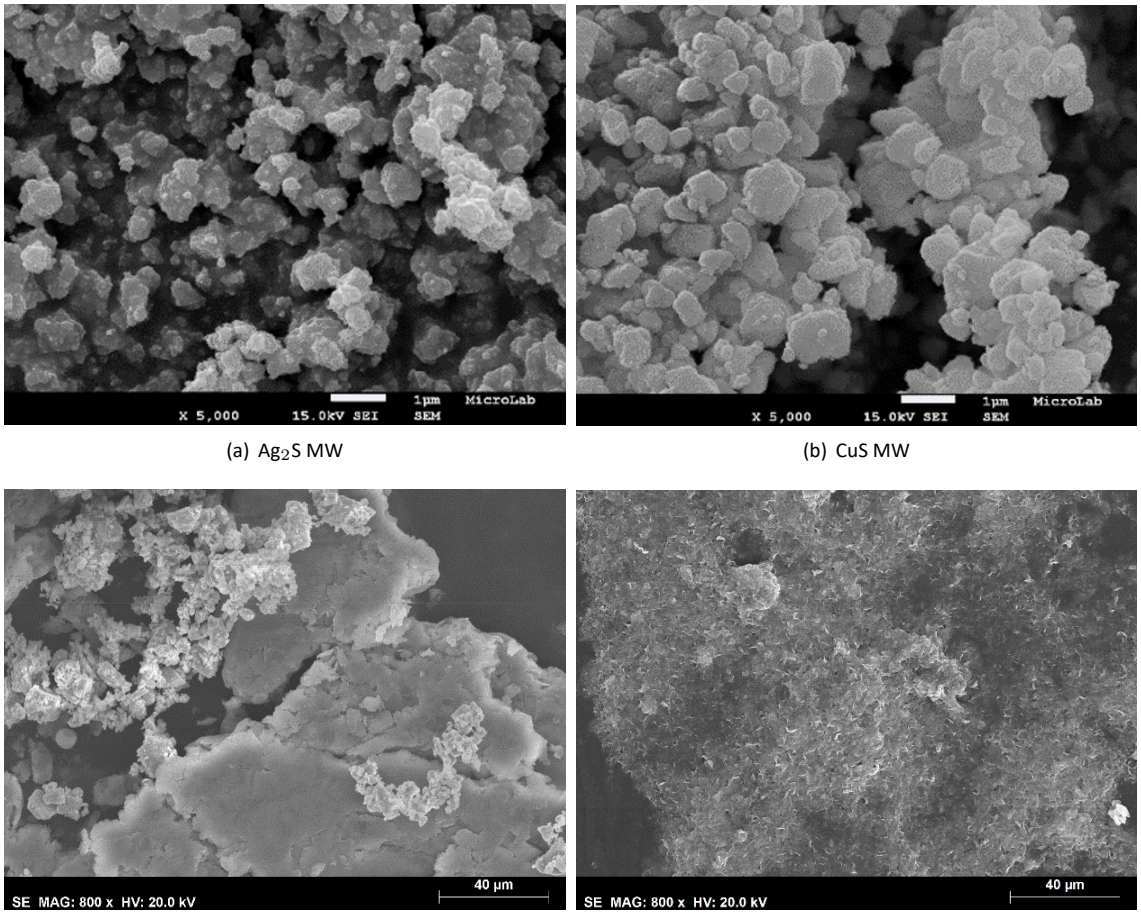

(a) Ag_2S MW

(b) CuS MW

(c) Ag_2S UI before sonication

(d) Ag_2S UI after sonication

Figure 3.13: (a) Ag_2S and (b) CuS nanoparticles obtained by microwave method; Ag_2S obtained via ultrasonic irradiation (c) before and (d) after sonication

3.2.2 Deposition Optimization

The first step on the study of the NPs films was to find the flow rate and applied voltage values that lead to the drop formation at the needle tip while using ethanol as a solvent. Then the distances bevel/ring and ring/target were also fixed. The influence of the dispersion concentration and the deposition time were explored. The concentrations used were 1, 2 and 4 mg/mL and the deposition times 3, 6 and 12 min.

Ag_2S UI nanoparticles were electrosprayed on 2.5 $\times$ 2.5 cm GZO 269 nm thick films deposited on glass(GZO200). As mentioned, these smaller samples were mounted on 10 $\times$ 10 cm aluminum foil covered glass. Since Ag_2S absorbs in the visible region and GZO does not, to be able to properly analyze the effect of concentration and time, the absorption and transmittance plots in the 200 - 1100 nm wavelengths range were studied (Figures 3.14 and 3.15).

The average sighted human eye is most sensitive to wavelengths around 550 nm. In view of that, the absorption at 550 nm from each graph was obtained and it is represented in Figure 3.16. As expected, overall, longer deposition times and the higher concentrations lead to higher absorptions. Though, for a short deposition time, 3 min, the concentration seems to have little influence on the absorption. Analyzing the trend of absorption spectra, it's possible to observe a linear dependence with the concentration and time. The greater and lowest values achieved were in the order of 22.5% and 5.8%. As the coating is

intended to have some transmittance, at least 60%, a film obtained with a concentration of 4 mg/mL and a time of 6 min with a ∼17% absorption (and ∼72% transmittance) at 550 nm seems reasonable to combine the TCO-metal structures studied previously.

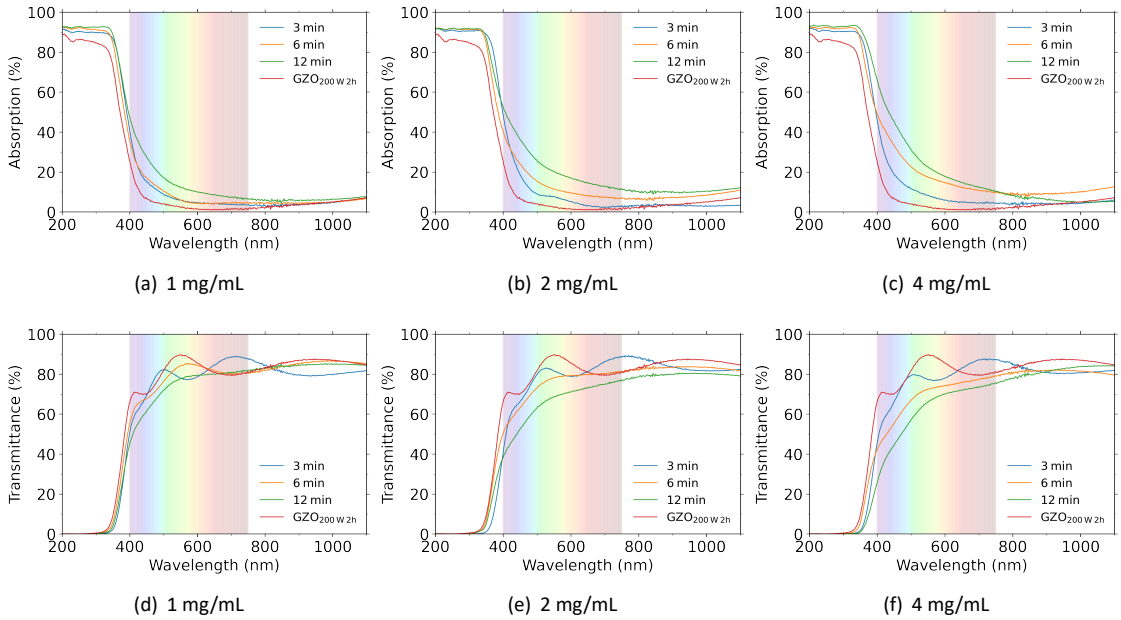

Figure 3.14: Time effect on Abs and T for different concentrations of Ag_2S UI deposited onto 269 nm thick GZO films (GZO200): 1 mg/mL, 2 mg/mL, 4 mg/mL

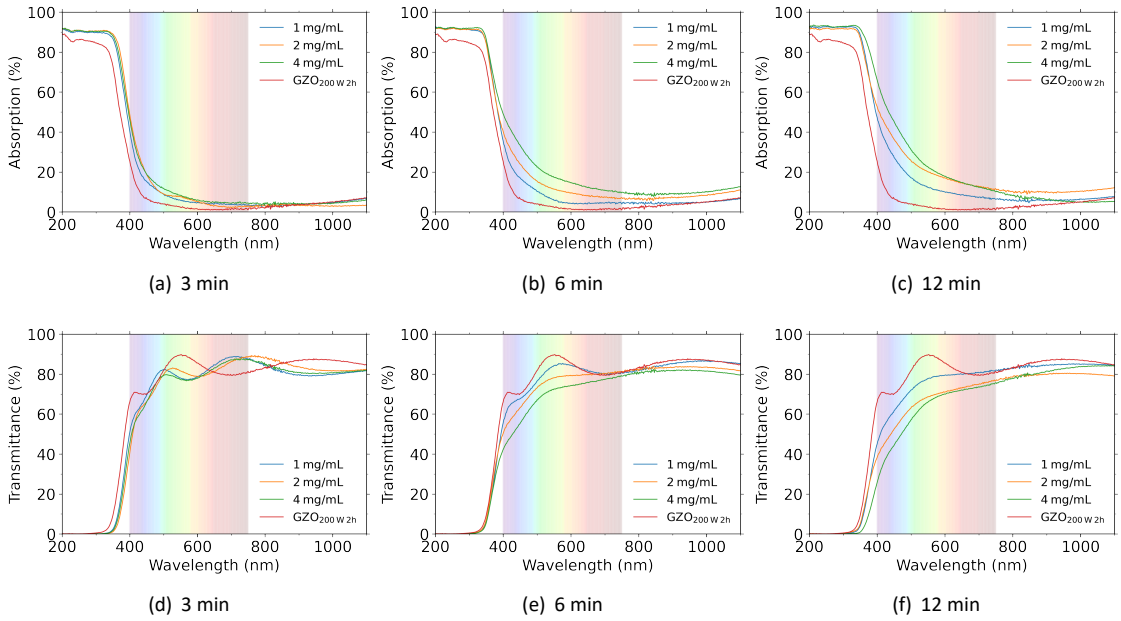

Figure 3.15: Concentration effect on Abs and T of Ag_2S UI deposited onto 269 nm thick GZO films (GZO200) for different deposition times: 3 min, 6 min, 12 min

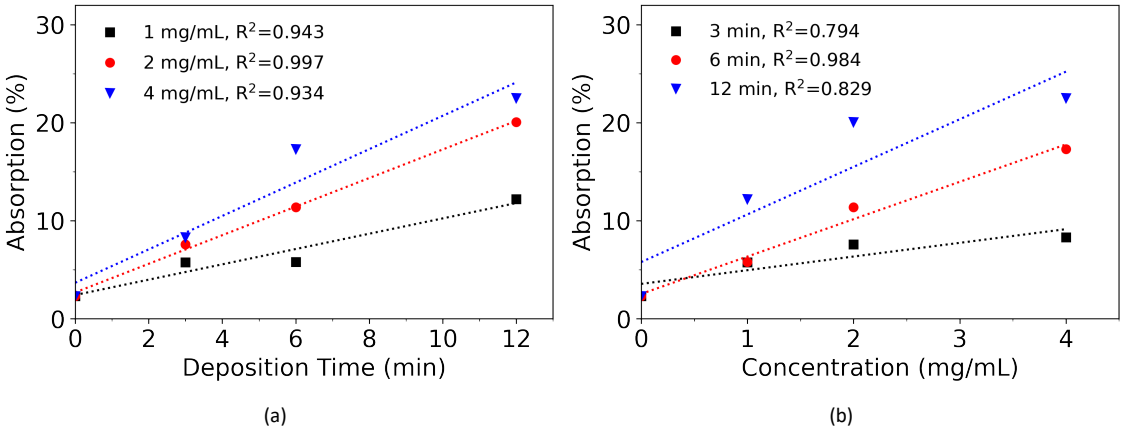

Figure 3.16: Absorption at 550 nm as a function of (a) deposition time and (b) concentration using GZO200 as substrate

3.2.3 Sulfide Films

The films were produced on 20 nm thick GZO films on glass substrates (GZO50) and the concentration of particles suspension was settled to 4mg/mL. Figure 3.17 shows the absorption spectra of glass/GZO without and with NPs deposited for 6 min. The studied nanoparticles are band gap materials and absorb near-infrared light. Unlike Ag_2S, the CuS appears to absorb in the NIR range at wavelengths above ∼1000 nm. The nanoparticles feature a broad LSPR in the NIR with a peak around 1500 nm. CuS has a p-type character and a plasmon resonance that absorbs significantly from 900 to 1600 nm, since the holes act as positive charge carriers [76]. With this in mind, the copper sulfide deposition was extended to 36 min. It can be seen that the film demonstrates a good IR blocking ability, though the band gap transition limits the development of films with adequate visible transmission.

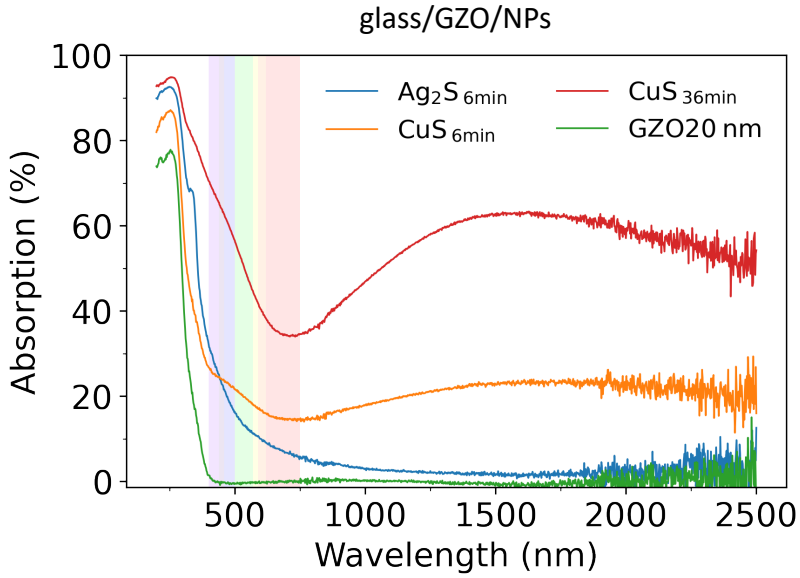

Figure 3.17: Absorption spectrum of silver and copper sulfide nanoparticles

The structural properties of nanoparticles films were investigated using XRD technique. In general, the XRD plot does not have any peaks or lines besides the ones attributed to the ZnO (34.45°), above 20°, or the broad peak at 24° due to glass substrate. Due to the scarcity of DRX patterns in the 10° to 20° in literature, we were unable to identify the peaks in Figure 3.18. The diffractogram of Ag_2S nanoparticles prepared by UI method shows in the left side peaks that may be attributed to an unexpected phase that couldn't be identified. But according to Match software a possibility would be a compound like silver ammonium nitrate ($AgH_4N_3O_6$).

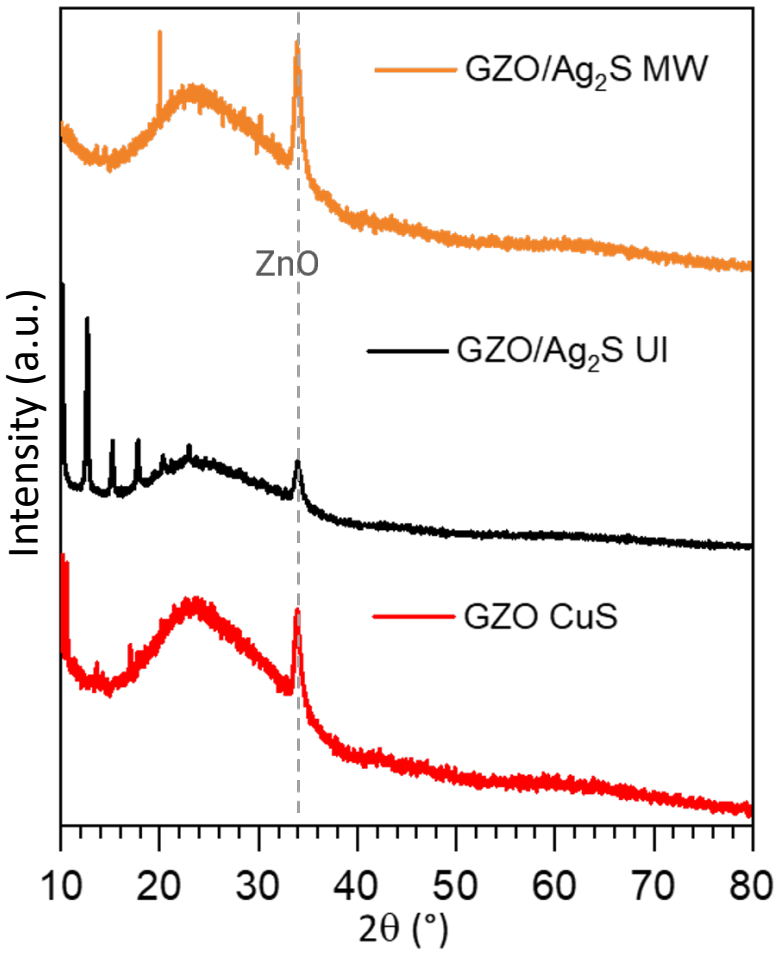

Figure 3.18: XRD of silver and copper sulfide films

3.2.4 Discussion

When comparing the NPs deposited on GZO films with different thicknesses, the 550 nm absorption for a 6 min deposition in GZO50 is around ∼17% as well (Figure 3.19(a)). However, one can observe that there was a considerable absorption increase for a higher deposition time from 22.5% to 35.9%. On the other hand, by using the CuS nanoparticles, the absorption spectra exhibited for the chosen parameters varies between 13.5% and 24.6% for different deposited films. Further systematic studies are needed for understanding process variation.

As ambient conditions during electrospray deposition affect the process itself [79], Table 3.4 summarizes these for the sample deposition in Figure 3.19(b). However, such difference can be due to a number of factors, in particular all that influence in the amount of NPs arriving to the GZO target, *e.g.*, NPs concentration in the solution, electric field instabilities, GZO films conductivity variation, which may be caused by a none-uniform areal thickness. For instance, target from Try 1, where less material has been deposited, corresponds to a corner of the GZO 20 nm thick where there is less sputtered TCO, and the resistance is too high to be measured. In this particular case, the substrate also has an impact since its conductivity influences the quantity of material that reaches it in a certain time. All these parameters are going to affect the optical spectrum since the film absorption depends on the volume of material deposited. These results thus need to be interpreted with caution.

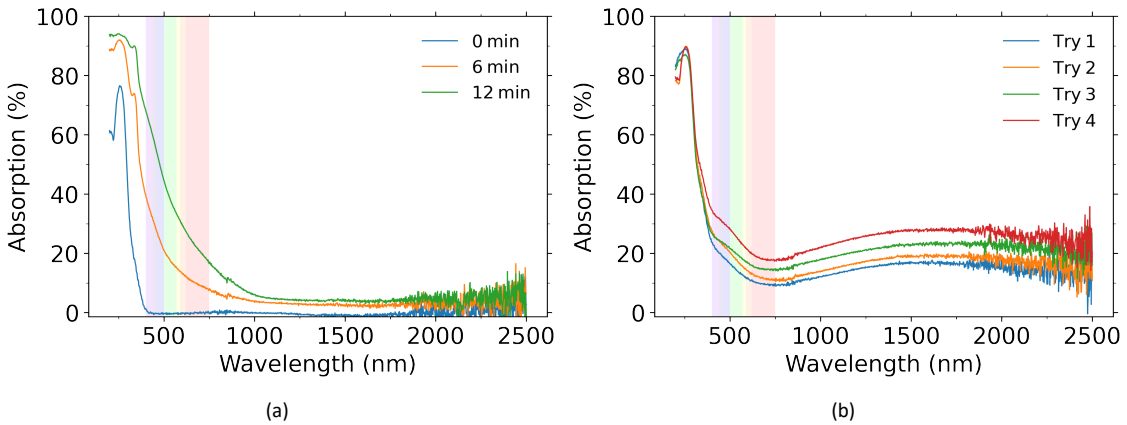

Figure 3.19: Absorption spectra of (a) Ag_2S with a concentration of 4 mg/mL and (b) of CuS nanoparticles deposited in the same concentration and time conditions.

Table 3.4: Temperature and humidity conditions for CuS nanoparticles deposited in the same concentration and time conditions

Try	Temperature / °C	Humidity / %
1	∼27	∼33
2	∼26	∼35
3	∼27	∼34
4	∼26	∼36

3.3 Metal-Oxide-NPs

This section presents the characterization of low-e structure developed with the produced nanoparticles. Then, NPs films were applied onto Cu and TCO substrates according to the deposition conditions presented on section 3.2.2. Hence, GZO/NPs coatings were developed. As already mentioned, the GZO top layer, when in contact with the metal, has anti-reflective properties, but this doesn't occur in the case of the nanoparticle coatings, there is an increase in band gap absorption which, as already noted, is shown to occur in the visible region. This is clearly illustrated in the figure 3.20

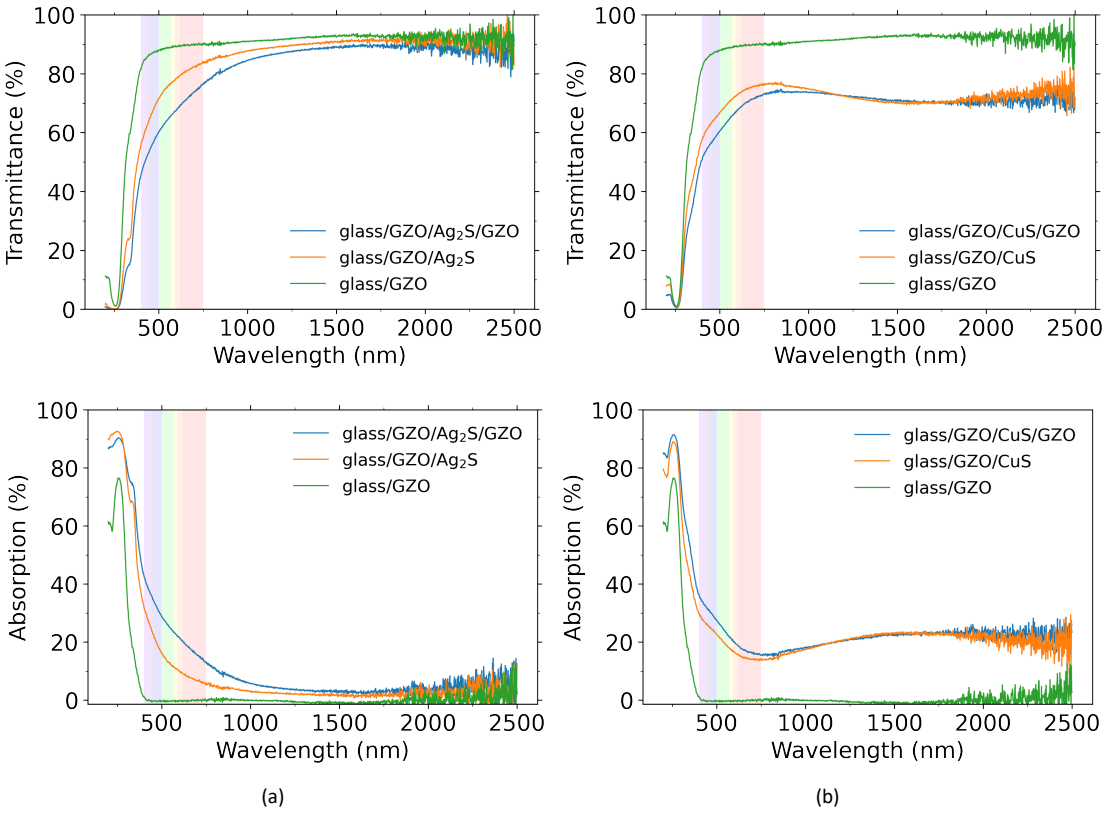

Figure 3.20: T and Abs spectra of Trilayer of (a) Ag_2S and (b) CuS

The introduction of the nanoparticles in the Cu structures increases the IR transmission, *i.e.*, causes the loss of their IR reflective properties (figure 3.21). In the the GZO sealed multilayers (glass/GZO/Cu/GZO and glass/GZO/Cu/NPs/GZO), the Ag_2S seems to have a more pronounced effect on transmittance spectra of the copper films, possibly because in the 'CuS films' occurs a higher IR absorption increase that compensates for the decrease in reflectance.

The NPs came off easily with mechanic action and the GZO didn't adhere when sputtered on top, which are obstacles to overcome in future work. A few attempts were made to try to improve nanoparticles adhesion to the substrate. One of them was to anneal the glass/GZO/CuS assembly at 200 °C, however, it did not work, and the IR absorption was lost. Another attempt was to increase the thickness of the GZO top layer (by increasing deposition time by 1 h) to see if it would completely cover the NPs, but it was not successful either. This problem can perhaps be overcome by using other deposition techniques or using a binder as authors Dwech, Aadim, and Hamid [80] and Chaudhuri and Patel [81] have done.

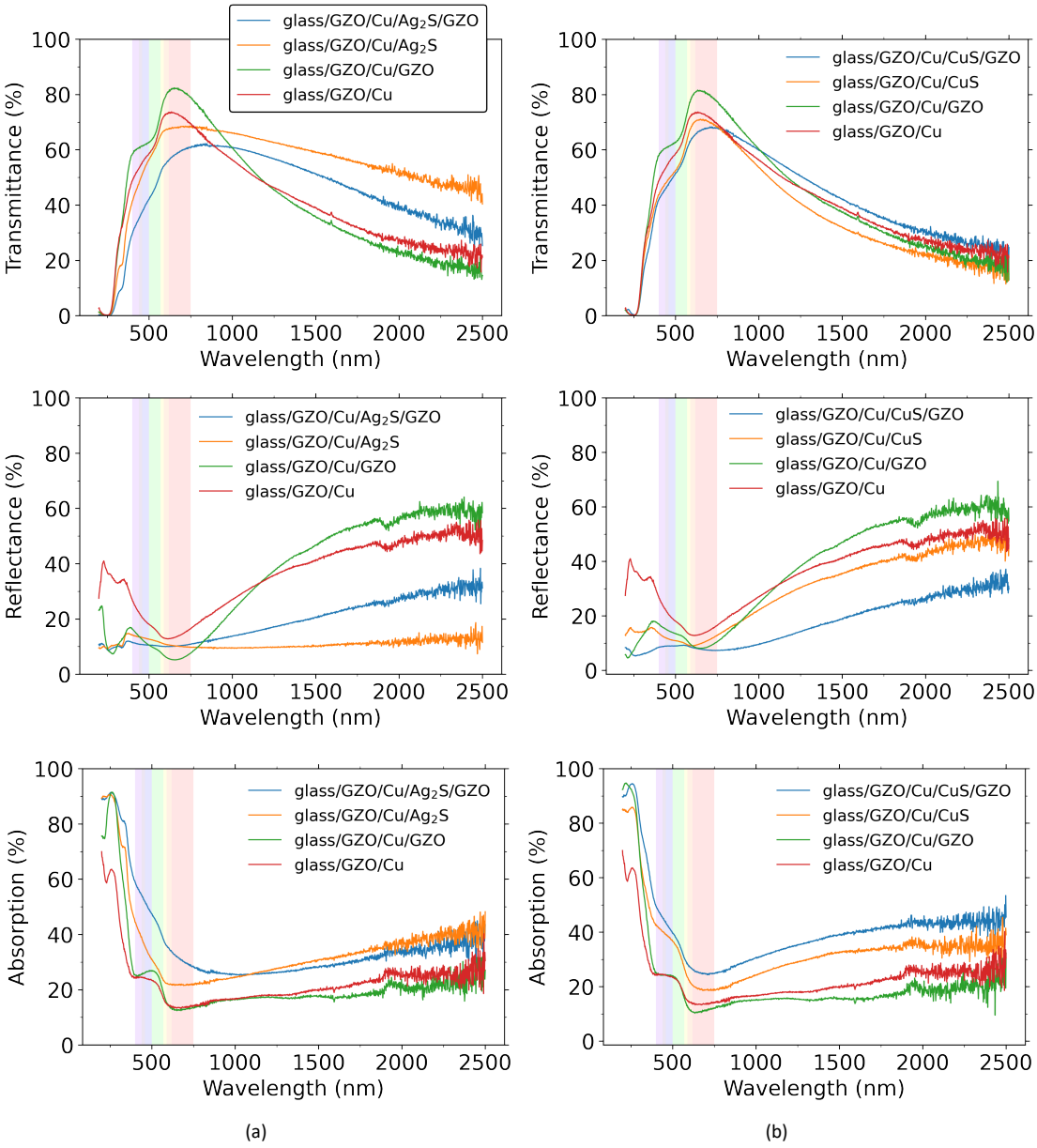

Figure 3.21: T, R and Abs spectra of of TCO/Metal/NPs films: (a) Ag_2S and (b) CuS

In summary, this section tried to improve the IR shielding ability of copper low-e structures around 800-1000 nm wavelengths by incorporating sulfide nanoparticles. Although they ended compromising the reflective properties, the fact that it was possible to deposit nanoparticles by the electrospray method is by itself an achievement.

4 Conclusion

Cu-based low emissivity coatings are being considered as an alternative to that Ag-based for their lower cost and durability to reflecting heat. Therefore, in the scope of this thesis a number of Cu-coatings have been produced and performance compared with that of Ag, so far more exploited and herein taken as reference. The standard Ag-coatings employ as transparent conductive oxides ITO but, in this thesis, GZO was used instead as it is cheaper and it has been used to produce low-e coatings.

GZO can be deposited by a number of techniques but herein sputtering deposition has been selected. As the optical properties are ruled by films thickness, density and stoichiometry, which can be affected by parameters, these were optimized and films composition, thickness and roughness were assessed by PIXE, RBS and AFM techniques and XRD for characterizing structural aspects of materials. The GZO films composition is consistent with the nominal compositions indicated by the supplier for GZO target and no contaminants were detected in the films by PIXE. Regarding GZO thickness optimization by sputtering for the development of low-emissivity coatings it was concluded that an optimal thickness may be in the range of 20 nm, which corresponds to an average roughness of 3.5 nm. The GZO crystallites in the samples had hexagonal wurtzite structure. Additionally, GZOs with thicknesses around 269 nm are revealed to be good candidates as plasmonic materials in the NIR region.

The low-e films were found to be efficient, with a temperature drop of approximately 20% in best result obtained: GZO/Ag/GZO. This coating presented a greater performance when compared to the GZO/Cu/GZO and was comparable to the ITO/Ag/ITO from a previous study, though the optical properties were slightly inferior. The silver structures presented higher Tvis and R in the NIR. Alternatively, still with the aim of increasing the GZO/Cu/GZO IR blocking and make their performance closer to that of GZO/Ag/GZO, the Cu-based coating was annealed at different temperatures (400 and 500 °C) and times (45 and 90 min). GZO-Cu structure needs annealing for enhancing optical properties, *i.e.*, visible transmittance, however results showed an increase in vis-IR shielding. The best combination proved to be 500 °C 45 min, but time and temperature still require further systematic optimization.

This work managed to successfully deposit the NPs on glass by electrospray. Since NIR-absorbing nanoparticles have been added to low-emissivity coatings as a route for achieving IR-shielding, CuS and Ag_2S nanoparticles have been used to develop GZO/Cu/NPs coatings and their optical performance further studied. Their optical properties revealed that adding the nanoparticles causes the films to lose their IR reflective properties and visible transmission. On the other hand, the copper sulfide shows potential as an IR shield, though the development of CuS films with adequate visible interval is severely limited by band gap transition as the absorption causes less visible light to be transmitted.

Bibliography

[1] E. Union. "Directive (EU) 2018/844 of the European Parliament and of the Council of 30 May 2018 amending Directive 2010/31/EU on the energy performance of buildings and Directive 2012/27/EU on energy efficiency". In: *Official Journal of the European Union* L156.75 (2018), pp. 156/75–156/91. ISSN: 16113349 (cit. on p. 1).

[2] G. Ding and C. Clavero. "Silver-Based Low-Emissivity Coating Technology for Energy- Saving Window Applications". In: *Modern Technologies for Creating the Thin-film Systems and Coatings* (2017). DOI: 10.5772/67085 (cit. on pp. 1, 2).

[3] B. P. Jelle, S. E. Kalnæs, and T. Gao. *Low-emissivity materials for building applications: A state-of-the-art review and future research perspectives*. Vol. 96. 2015, pp. 329–356. ISBN: 4773593377. DOI: 10.1016/j.enbuild.2015.03.024 (cit. on pp. 1, 3).

[4] S. Termkleebbuppa et al. "Copper-Zinc Oxide Synergistic Approach as Low-Emissivity Material for Energy-Saving Windows". In: *IOP Conference Series: Materials Science and Engineering* 811.1 (May 2020), p. 012010. ISSN: 1757899X. DOI: 10.1088/1757-899X/811/1/012010. URL: https://iopscience.iop.org/article/10.1088/1757-899X/811/1/012010 (cit. on p. 1).

[5] G. K. Dalapati et al. "Transparent heat regulating (THR) materials and coatings for energy saving window applications: Impact of materials design, micro-structural, and interface quality on the THR performance". In: *Progress in Materials Science* 95 (2018), pp. 42–131. ISSN: 00796425. DOI: 10.1016/j.pmatsci.2018.02.007. URL: http://dx.doi.org/10.1016/j.pmatsci.2018.02.007 (cit. on pp. 1–3).

[6] E. H. Nezhad, H. Haratizadeh, and B. M. Kari. "Influence of Ag mid-layer in the optical and thermal properties of ZnO/Ag/ZnO thin films on the glass used in Buildings as insulating glass unit (IGU)". In: *Ceramics International* 45.8 (2019), pp. 9950–9954. ISSN: 02728842. DOI: 10.1016/j.ceramint.2019.02.037. URL: https://doi.org/10.1016/j.ceramint.2019.02.037 (cit. on pp. 1–3, 13).

[7] Y. Ma et al. "TiN-based organic-inorganic composite films with dual functions of solar control and low-emission for energy-saving coatings". In: *Materials Research Express* 7.6 (2020), pp. 0–12. ISSN: 20531591. DOI: 10.1088/2053-1591/ab96fd (cit. on p. 1).

[8] L. Holland and G. Siddall. "Heat-reflecting windows using gold and bismuth oxide films". In: *British Journal of Applied Physics* 9.9 (1958), pp. 359–361. ISSN: 05083443. DOI: 10.1088/0508-3443/9/9/304 (cit. on p. 1).

[9] B. Cai, R. Xin, and X. Jia. "The study of sputtered silver-based low-emissivity coating on glass". In: *Advanced Materials Research* 150-151 (2011), pp. 36–39. ISSN: 10226680. DOI: 10.4028/www.scientific.net/AMR.150-151.36 (cit. on pp. 1, 2).

[10] C. Zhang et al. "The enhancement of thermal endurance in doped low emissive ZnO/Ag/ZnO multilayer thin film". In: *Journal of Alloys and Compounds* 832 (2020), p. 154983. ISSN: 09258388. DOI: 10.1016/j.jallcom.2020.154983. URL: https://doi.org/10.1016/j.jallcom.2020.154983 (cit. on pp. 1–4).

[11] G. K. Dalapati et al. "Color tunable low cost transparent heat reflector using copper and titanium oxide for energy saving application". In: *Scientific Reports* 6.1 (Feb. 2016), pp. 1–14. ISSN: 20452322. DOI: 10.1038/srep20182. URL: www.nature.com/scientificreports (cit. on pp. 1, 2, 4, 11, 13).

[12] S. S. S. S. Kim et al. “Effect of rapid and selective thermal processing (RSTP) assisted by microwave treatment on the properties of ultrathin Ag-layer-inserted dielectric multilayers for low-emissivity glass”. In: *Japanese Journal of Applied Physics* 58.SE (2019), pp. 1–7. ISSN: 13474065. DOI: 10.7567/1347-4065/ab0c73. URL: https://doi.org/10.7567/1347-4065/ab0c73 (cit. on pp. 2, 4).

[13] N. Akin Sonmez et al. “Ag/M-seed/AZO/glass structures for low-E glass: Effects of metal seeds”. In: *International Journal of Applied Glass Science* 9.3 (2018), pp. 383–391. ISSN: 20411294. DOI: 10.1111/ijag.12331 (cit. on pp. 2, 3, 14).

[14] K. Sun et al. “Preparation and performance of low-emissivity Al-doped ZnO films for energy-saving glass”. In: *Ceramics International* 44.16 (2018), pp. 19597–19602. ISSN: 02728842. DOI: 10.1016/j.ceramint.2018.07.207. URL: https://doi.org/10.1016/j.ceramint.2018.07.207 (cit. on pp. 2, 4).

[15] M. B. Cinali and Ö. D. Coşkun. “Optimization of physical properties of sputtered silver films by change of deposition power for low emissivity applications”. In: *Journal of Alloys and Compounds* 853 (2021). ISSN: 09258388. DOI: 10.1016/j.jallcom.2020.157073 (cit. on pp. 2, 4).

[16] D. Miao et al. “Characterization of AZO and Ag based films prepared by RF magnetron sputtering”. In: *Journal of Alloys and Compounds* 616 (2014), pp. 26–31. ISSN: 09258388. DOI: 10.1016/j.jallcom.2014.07.105. URL: http://dx.doi.org/10.1016/j.jallcom.2014.07.105 (cit. on p. 2).

[17] K. Gao et al. “Reduced thermal effect of AZO/Cu/AZO infrared filter film for solar cell”. In: *Optical Materials* 110.October (2020), p. 110534. ISSN: 09253467. DOI: 10.1016/j.optmat.2020.110534. URL: https://doi.org/10.1016/j.optmat.2020.110534 (cit. on p. 2).

[18] S. H. Kim, S. H. Kim, and P. K. Song. “Near infrared reflecting properties of TiO2/Ag/TiO2 multilayers prepared by DC/RF magnetron sputtering”. In: *Journal of Korean Institute of Metals and Materials* 55.8 (2017), pp. 581–586. ISSN: 17388228. DOI: 10.3365/KJMM.2017.55.8.581 (cit. on pp. 2, 15).

[19] M. F. Al-Kuhaili et al. “Energy-saving transparent heat mirrors based on tungsten oxide-gold WO 3/Au/WO 3 multilayer structures”. In: *Solar Energy* 86.11 (2012), pp. 3183–3189. ISSN: 0038092X. DOI: 10.1016/j.solener.2012.08.008. URL: http://dx.doi.org/10.1016/j.solener.2012.08.008 (cit. on p. 2).

[20] R. Harakat Mohsin, M. K. Khalaf, and A. N. Al-Gaffer. “Multilayer coatings D/M/D for solar reflector applications prepared by DC magnetron sputtering”. In: *AIP Conference Proceedings* 2213.March (2020). ISSN: 15517616. DOI: 10.1063/5.0000449 (cit. on pp. 2, 3, 13).

[21] M. Yuste et al. “Improving the visible transmittance of low-e titanium nitride based coatings for solar thermal applications”. In: *Applied Surface Science* 258.5 (2011), pp. 1784–1788. ISSN: 01694332. DOI: 10.1016/j.apsusc.2011.10.046. URL: http://dx.doi.org/10.1016/j.apsusc.2011.10.046 (cit. on p. 2).

[22] A. Mallick, S. Ghosh, and D. Basak. “Highly conducting and transparent low-E window films with high figure of merit values based on RF sputtered Al and In co-doped ZnO”. In: *Materials Science in Semiconductor Processing* 119.July (2020), p. 105240. ISSN: 13698001. DOI: 10.1016/j.mssp.2020.105240. URL: https://doi.org/10.1016/j.mssp.2020.105240 (cit. on p. 2).

[23] L. Gong et al. “Highly transparent conductive and near-infrared reflective ZnO:Al thin films”. In: *Vacuum* 84.7 (2010), pp. 947–952. ISSN: 0042207X. DOI: 10.1016/j.vacuum.2010.01.010. URL: http://dx.doi.org/10.1016/j.vacuum.2010.01.010 (cit. on p. 2).

[24] C. Guillén and J. Herrero. "TCO/metal/TCO structures for energy and flexible electronics". In: *Thin Solid Films* 520.1 (2011), pp. 1–17. ISSN: 00406090. DOI: 10.1016/j.tsf.2011.06.091. URL: http://dx.doi.org/10.1016/j.tsf.2011.06.091 (cit. on pp. 2–4, 10).

[25] C. Bianchi et al. "Near Infrared Photothermoelectric Effect in Transparent AZO / ITO / Ag / ITO Thin Films". In: (2021), pp. 1–20 (cit. on pp. 2, 10, 13).

[26] C. Zhang et al. "Thin-Metal-Film-Based Transparent Conductors: Material Preparation, Optical Design, and Device Applications". In: *Advanced Optical Materials* 2001298 (2020), pp. 1–40. ISSN: 21951071. DOI: 10.1002/adom.202001298 (cit. on pp. 2–4).

[27] D. Miao et al. "Infrared reflective properties of AZO/Ag/AZO trilayers prepared by RF magnetron sputtering". In: *Ceramics International* 40.8 PART B (2014), pp. 12847–12853. ISSN: 02728842. DOI: 10.1016/j.ceramint.2014.04.139. URL: http://dx.doi.org/10.1016/j.ceramint.2014.04.139 (cit. on p. 2).

[28] C. C. Wu et al. "TiOx/Ag/TiOx multilayer for application as a transparent conductive electrode and heat mirror". In: *Journal of Materials Science: Materials in Electronics* 24.7 (2013), pp. 2461–2468. ISSN: 09574522. DOI: 10.1007/s10854-013-1118-1 (cit. on pp. 2, 14).

[29] H. Ferhati and F. Djeffal. "Performance assessment of TCO/metal/TCO multilayer transparent electrodes: from design concept to optimization". In: *Journal of Computational Electronics* 19.2 (2020), pp. 815–824. ISSN: 15728137. DOI: 10.1007/s10825-020-01459-9. URL: https://doi.org/10.1007/s10825-020-01459-9 (cit. on pp. 3, 10).

[30] J. Ho Kim et al. "Al-doped ZnO/Ag/Al-doped ZnO multilayer films with a high figure of merit". In: *Ceramics International* 41.10 (2015), pp. 14805–14810. ISSN: 02728842. DOI: 10.1016/j.ceramint.2015.08.001 (cit. on p. 3).

[31] S. Van Eek et al. "Investigation of material properties and thermal stabilities of magnetron-sputter-deposited ZnO:Al/Ag/ZnO:Al transparent conductive coatings for thin-film solar cell applications". In: *Japanese Journal of Applied Physics* 56.8 (2017). ISSN: 13474065. DOI: 10.7567/JJAP.56.08MA12 (cit. on p. 3).

[32] O. Adedokun. "Review on Transparent Conductive Oxides Thin Films deposited by Sol-gel spin coating technique". In: *International Journal of Engineering Science and Application* 2.3 (2018), pp. 88–97. URL: https://dergipark.org.tr/ijesa/issue/39397/427973 (cit. on p. 3).

[33] M. Gabás et al. "High quality ZnO and Ga:ZnO thin films grown onto crystalline Si (1 0 0) by RF magnetron sputtering". In: *Solar Energy Materials and Solar Cells* 95.8 (2011), pp. 2327–2334. ISSN: 09270248. DOI: 10.1016/j.solmat.2011.04.001 (cit. on p. 3).

[34] T. Hirano et al. "Influence of aluminum interlayer on optical properties of very thin silver thin film". In: *Surface and Coatings Technology* 393.November 2019 (2020), p. 125752. ISSN: 02578972. DOI: 10.1016/j.surfcoat.2020.125752. URL: https://doi.org/10.1016/j.surfcoat.2020.125752 (cit. on p. 3).

[35] Y. El Mouedden et al. "Thin film coatings for solar and thermal radiation control prepared by physical vapour deposition". In: *2012 9th International Conference on High Capacity Optical Networks and Enabling Technologies, HONET 2012* (2012), pp. 83–86. DOI: 10.1109/HONET.2012.6421440 (cit. on pp. 3, 4).

[36] P. Panprom et al. “Growth of Ag/SnO2 thin film by DC magnetron sputtering deposition intended for low emissivity application”. In: *AIP Conference Proceedings* 2010.1 (Sept. 2018), p. 20028. ISSN: 0094-243X. DOI: 10.1063/1.5053204. URL: https://doi.org/10.1063/1.5053204%20https://aip.scitation.org/doi/abs/10.1063/1.5053204 (cit. on p. 4).

[37] R. Soltanmoradi et al. “Near-infrared light absorption and scattering based on a mono-layer of gold nanoparticles”. In: *Journal of the European Optical Society* 10 (2015). ISSN: 19902573. DOI: 10.2971/jeos.2015.15031 (cit. on p. 5).

[38] A. M. Gobin et al. “Near-infrared-resonant gold/gold sulfide nanoparticles as a photothermal cancer therapeutic agent”. In: *Small* 6.6 (2010), pp. 745–752. ISSN: 16136810. DOI: 10.1002/smll.200901557 (cit. on p. 5).

[39] A. A. Rokade, Y. E. Jin, and S. S. Park. “Facile synthesis of plate-like CuS nanoparticles and their optical and photo-thermal properties”. In: *Materials Chemistry and Physics* 207 (2018), pp. 465–469. ISSN: 02540584. DOI: 10.1016/j.matchemphys.2017.12.077. URL: https://doi.org/10.1016/j.matchemphys.2017.12.077 (cit. on p. 5).

[40] W. Zhong et al. “Synthesis of CuS nanoplate-containing PDMS film with excellent near-infrared shielding properties”. In: *RSC Advances* 6.23 (2016), pp. 18881–18890. ISSN: 20462069. DOI: 10.1039/c5ra22611b. URL: http://dx.doi.org/10.1039/C5RA22611B (cit. on p. 5).

[41] Z. Zhao et al. “Csx WO3 nanoparticles for the near-infrared shielding film”. In: *Journal of Nanoscience and Nanotechnology* 15.9 (2015), pp. 7173–7176. ISSN: 15334899. DOI: 10.1166/jnn.2015.10536 (cit. on p. 5).

[42] Y. Yao et al. “Synthesis of CsxWO3 nanoparticles and their NIR shielding properties”. In: *Ceramics International* 44.12 (2018), pp. 13469–13475. ISSN: 02728842. DOI: 10.1016/j.ceramint.2018.04.158. URL: https://doi.org/10.1016/j.ceramint.2018.04.158 (cit. on p. 5).

[43] H. Takeda and K. Adachi. “Near infrared absorption of tungsten oxide nanoparticle dispersions”. In: *Journal of the American Ceramic Society* 90.12 (2007), pp. 4059–4061. ISSN: 00027820. DOI: 10.1111/j.1551-2916.2007.02065.x (cit. on p. 5).

[44] T. M. Liu et al. *Revisiting the classification of NIR-absorbing/emitting nanomaterials for in vivo bioapplications*. 2016. DOI: 10.1038/am.2016.106. URL: www.nature.com/am (cit. on p. 5).

[45] D. Miao et al. “Highly transparent and infrared reflective AZO/Ag/AZO multilayer film prepared on PET substrate by RF magnetron sputtering”. In: *Vacuum* 106 (2014), pp. 1–4. ISSN: 0042207X. DOI: 10.1016/j.vacuum.2014.02.021. URL: http://dx.doi.org/10.1016/j.vacuum.2014.02.021 (cit. on p. 5).

[46] D. Gaspar et al. “Ag and Sn Nanoparticles to Enhance the Near-Infrared Absorbance of a-Si:H Thin Films”. In: *Plasmonics* 9.5 (2014), pp. 1015–1023. ISSN: 15571963. DOI: 10.1007/s11468-014-9709-0 (cit. on p. 5).

[47] H. N. Kim and S. Yang. “Responsive Smart Windows from Nanoparticle–Polymer Composites”. In: *Advanced Functional Materials* 30.2 (2020), pp. 1–25. ISSN: 16163028. DOI: 10.1002/adfm.201902597 (cit. on p. 5).

[48] S. D. Lounis et al. “Defect chemistry and Plasmon physics of colloidal metal oxide Nanocrystals”. In: *Journal of Physical Chemistry Letters* 5.9 (2014), pp. 1564–1574. ISSN: 19487185. DOI: 10.1021/jz500440e (cit. on p. 5).

[49] L. V. Besteiro et al. “Plasmonic Glasses and Films Based on Alternative Inexpensive Materials for Blocking Infrared Radiation”. In: *Nano Letters* 18.5 (2018), pp. 3147–3156. ISSN: 15306992. DOI: 10.1021/acs.nanolett.8b00764 (cit. on p. 5).

[50] K. Manthiram and A. P. Alivisatos. “Tunable localized surface plasmon resonances in tungsten oxide nanocrystals”. In: *Journal of the American Chemical Society* 134.9 (2012), pp. 3995–3998. ISSN: 00027863. DOI: 10.1021/ja211363w (cit. on p. 5).

[51] J. T. Jørgensen et al. “Single Particle and PET-based Platform for Identifying Optimal Plasmonic Nano-Heaters for Photothermal Cancer Therapy”. In: *Scientific Reports* 6.August (2016), pp. 1–10. ISSN: 20452322. DOI: 10.1038/srep30076. URL: http://dx.doi.org/10.1038/srep30076 (cit. on p. 5).

[52] H. Roshan et al. “High-detectivity near-infrared photodetector based on Ag2S nanocrystals”. In: *Journal of Alloys and Compounds* 852 (2021), p. 156948. ISSN: 09258388. DOI: 10.1016/j.jallcom.2020.156948. URL: https://doi.org/10.1016/j.jallcom.2020.156948 (cit. on p. 5).

[53] J. Fang et al. “Hydrothermal synthesis of nanostructured CuS for broadband efficient optical absorption and high-performance photo-thermal conversion”. In: *Solar Energy Materials and Solar Cells* 185.May (2018), pp. 456–463. ISSN: 09270248. DOI: 10.1016/j.solmat.2018.05.060. URL: https://doi.org/10.1016/j.solmat.2018.05.060 (cit. on p. 5).

[54] R. Zamiri et al. “The structural and optical constants of Ag2S semiconductor nanostructure in the Far-Infrared”. In: *Chemistry Central Journal* 9.1 (2015), pp. 4–9. ISSN: 1752153X. DOI: 10.1186/s13065-015-0099-y. URL: http://dx.doi.org/10.1186/s13065-015-0099-y (cit. on p. 5).

[55] J. O. Adeyemi, O. A. Oyewo, and D. C. Onwudiwe. “Optical and Structural Properties of Tin Sulfide Nanoparticles Obtained via Solvothermal Routes”. In: *Zeitschrift fur Anorganische und Allgemeine Chemie* 645.15 (2019), pp. 998–1003. ISSN: 15213749. DOI: 10.1002/zaac.201900065 (cit. on p. 5).

[56] S. Sohila et al. “Optical and Raman scattering studies on SnS nanoparticles”. In: *Journal of Alloys and Compounds* 509.19 (2011), pp. 5843–5847. ISSN: 09258388. DOI: 10.1016/j.jallcom.2011.02.141. URL: http://dx.doi.org/10.1016/j.jallcom.2011.02.141 (cit. on p. 5).

[57] N. Rafiq et al. “Structural, thermal and optical investigation of tin sulfide nanoparticles for next-generation photovoltaic applications”. In: *Materials Science- Poland* 36.2 (2018), pp. 270–275. ISSN: 2083134X. DOI: 10.1515/msp-2018-0042 (cit. on p. 5).

[58] D. Magalhães Sousa et al. “Microwave Synthesis of Silver Sulfide and Silver Nanoparticles: Light and Time Influence”. In: *ACS Omega* 5.22 (June 2020), pp. 12877–12881. ISSN: 24701343. DOI: 10.1021/acsomega.0c00656 (cit. on p. 6).

[59] M. H. Kang et al. “Synthesis of silver sulfide nanoparticles and their photodetector applications”. In: *RSC Advances* 8.50 (2018), pp. 28447–28452. ISSN: 20462069. DOI: 10.1039/c8ra03306d (cit. on p. 6).

[60] E. Nastasi, Y. Wang. *Handbook of Modern Ion Beam Analysis*. 2009, p. 370. ISBN: 9781605112176 (cit. on p. 7).

[61] R. Van Grieken. “Particle-induced X-Ray emission spectrometry (PIXE)”. In: *TrAC Trends in Analytical Chemistry* 16.2 (1997), pp. VIII–IX. ISSN: 01659936. DOI: 10.1016/s0165-9936(97)81471-9 (cit. on p. 7).

[62] J. Loureiro et al. “Improved thermoelectric properties of nanocrystalline hydrogenated silicon thin films by post-deposition thermal annealing”. In: *Thin Solid Films* 642.September (2017), pp. 276–280. ISSN: 00406090. DOI: 10.1016/j.tsf.2017.09.047. URL: http://dx.doi.org/10.1016/j.tsf.2017.09.047 (cit. on p. 7).

[63] P. Sakthivel et al. “Influence of radiofrequency power on structural, morphological, optical and electrical properties of magnetron sputtered CdO: Sm thin films as alternative TCO for optoelectronic applications”. In: *Journal of Alloys and Compounds* 765 (2018), pp. 146–157. ISSN: 09258388. DOI: 10.1016/j.jallcom.2018.06.215. URL: https://doi.org/10.1016/j.jallcom.2018.06.215 (cit. on pp. 8, 9).

[64] X. Hu et al. “Highly transparent superhydrophilic graphene oxide coating for antifogging”. In: *Materials Letters* 182 (2016), pp. 372–375. ISSN: 18734979. DOI: 10.1016/j.matlet.2016.06.125. URL: http://dx.doi.org/10.1016/j.matlet.2016.06.125 (cit. on p. 9).

[65] A. S. Pugalenthi et al. “Effect of thickness on the structural, optical and electrical properties of RF magnetron sputtered GZO thin films”. In: *Materials Science in Semiconductor Processing* 29 (2015), pp. 176–182. ISSN: 13698001. DOI: 10.1016/j.mssp.2014.02.014. URL: http://dx.doi.org/10.1016/j.mssp.2014.02.014 (cit. on p. 10).

[66] C. Zhu et al. “Tailoring the resonance wavelength and loss of highly Ga doped ZnO plasmonic materials by varied doping content and substrate temperature”. In: *Thin Solid Films* 605 (2016), pp. 95–101. ISSN: 00406090. DOI: 10.1016/j.tsf.2015.11.005. URL: http://dx.doi.org/10.1016/j.tsf.2015.11.005 (cit. on p. 10).

[67] C. H. Chu, H. W. Wu, and J. L. Huang. “Study of Cu-based Al-doped ZnO multilayer thin films with different annealing conditions”. In: *Ceramics International* 42.5 (2016), pp. 5754–5761. ISSN: 02728842. DOI: 10.1016/j.ceramint.2015.12.112. URL: http://dx.doi.org/10.1016/j.ceramint.2015.12.112 (cit. on p. 11).

[68] J. G. Lu et al. “Transparent conductive and near-infrared reflective Ga-doped ZnO/Cu bilayer films grown at room temperature”. In: *Journal of Vacuum Science & Technology A: Vacuum, Surfaces, and Films* 29.3 (2011), 03A115. ISSN: 0734-2101. DOI: 10.1116/1.3570864 (cit. on p. 11).

[69] J. Peng et al. “Transparent TiO2/Cu/TiO2 multilayer for electrothermal application”. In: *Materials* 14.4 (2021), pp. 1–10. ISSN: 19961944. DOI: 10.3390/ma14041024 (cit. on p. 11).

[70] M. Achintha. “Sustainability of glass in construction”. In: *Sustainability of Construction Materials*. Woodhead Publishing, Jan. 2016, pp. 79–104. DOI: 10.1016/b978-0-08-100370-1.00005-6 (cit. on p. 13).

[71] T. Chen, C. C. Chiang, and T. Y. Chen. “The characteristic of GZO thin film deposited on flexible substrates by using RF magnetron sputtering”. In: *Proceedings of AM-FPD 2014 - The 21st International Workshop on Active-Matrix Flatpanel Displays and Devices: TFT Technologies and FPD Materials* (2014), pp. 199–202. DOI: 10.1109/AM-FPD.2014.6867170 (cit. on p. 14).

[72] Y. P. Wang et al. “Transparent conductive and near-infrared reflective Cu-based Al-doped ZnO multilayer films grown by magnetron sputtering at room temperature”. In: *Applied Surface Science* 257.14 (2011), pp. 5966–5971. ISSN: 01694332. DOI: 10.1016/j.apsusc.2011.01.068 (cit. on p. 14).

[73] O. Alekperov, Z. Jahangirli, and R. Paucar. “First-principles lattice dynamics and Raman scattering in ionic conductor β-Ag2S”. In: *Physica Status Solidi (B) Basic Research* 253.10 (2016), pp. 2049–2055. ISSN: 15213951. DOI: 10.1002/pssb.201552784 (cit. on p. 17).

[74] S. H. Chaki, J. P. Tailor, and M. P. Deshpande. “Covellite CuS - Single crystal growth by chemical vapour transport (CVT) technique and characterization”. In: *Materials Science in Semiconductor Processing* 27.1 (2014), pp. 577–585. ISSN: 13698001. DOI: 10.1016/j.mssp.2014.07.038. URL: http://dx.doi.org/10.1016/j.mssp.2014.07.038 (cit. on p. 17).

[75] P. E. Rodríguez-Hernández et al. “Effect of laser fluence on structural and optical properties of CuxS films grown by pulsed laser deposition at different wavelengths”. In: *Materials Research Express* 7.1 (2020), pp. 0–10. ISSN: 20531591. DOI: 10.1088/2053-1591/ab663d (cit. on p. 17).

[76] N. J. Spear et al. “Enhanced Broadband and Harmonic Upconversion from Coupled Semiconductor and Metal Nanoparticle Films”. In: *ACS Applied Nano Materials* 3.4 (2020), pp. 3144–3150. ISSN: 25740970. DOI: 10.1021/acsanm.0c00064 (cit. on pp. 17, 21).

[77] W. Van Der Stam et al. “Switching between Plasmonic and Fluorescent Copper Sulfide Nanocrystals”. In: *Journal of the American Chemical Society* 139.37 (Sept. 2017), pp. 13208–13217. ISSN: 15205126. DOI: 10.1021/jacs.7b07788 (cit. on p. 17).

[78] A. Nath and A. Khare. “Size induced structural modifications in copper oxide nanoparticles synthesized via laser ablation in liquids”. In: *Journal of Applied Physics* 110.4 (2011). ISSN: 00218979. DOI: 10.1063/1.3626463 (cit. on p. 17).

[79] E. Assadpour and S. M. Jafari. *An overview of specialized equipment for nanoencapsulation of food ingredients*. Elsevier Inc., 2019, pp. 1–30. ISBN: 9780128156711. DOI: 10.1016/B978-0-12-815671-1.00001-9. URL: http://dx.doi.org/10.1016/B978-0-12-815671-1.00001-9 (cit. on p. 23).

[80] M. H. Dwech, K. A. Aadim, and L. A. Hamid. “Influence of laser energy on the characteristics of Ag2S/ITO thin films solar cell prepared by PLD technique”. In: *AIP Conference Proceedings* 2213.March (2020). ISSN: 15517616. DOI: 10.1063/5.0000029 (cit. on p. 24).

[81] T. K. Chaudhuri and M. G. Patel. “High refractive index films of ZnS/PVP nanocomposite by in situ thermolysis”. In: *Journal of Experimental Nanoscience* 10.2 (2015), pp. 135–147. ISSN: 17458099. DOI: 10.1080/17458080.2013.803615 (cit. on p. 24).

A Preliminary results

The first GZO/metal/GZO structures produced employed GZO films deposited on glass by sputtering with a power of 200 W for 2 h (GZO200). However, as shown figure A.1 Cu came off when the upper layer of GZO was deposited, which suggested that the deposition power was too high. Furthermore, the GZO thickness was too high, as the visible transmittance of the silver structures decreased. According to the RBS measurements shown ahead the thickness of each GZO film was 269 nm. The subsequent annealing, which was intended to raise the Tvis, also failed to be effective (figure A.2). Therefore, it was concluded that the aforementioned GZO was not compatible with the desired application.

Figure A.1: Photos of pilled-off GZO200/Cu/GZO200 after GZO deposition on Cu layer (left) and of GZO200/Ag/GZO200 (right)

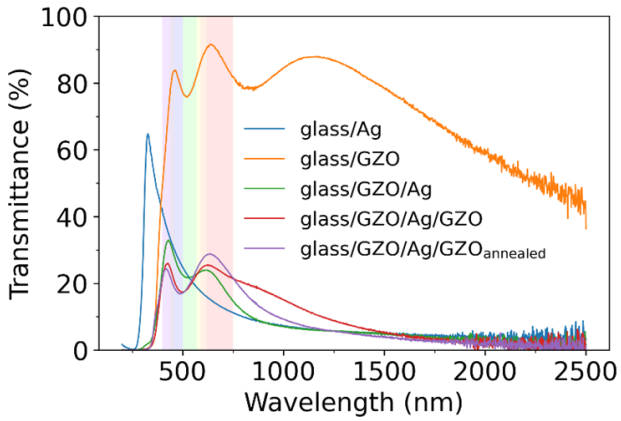

Figure A.2: Transmittance of GZO200 and Ag structures

B Electrospray Setup

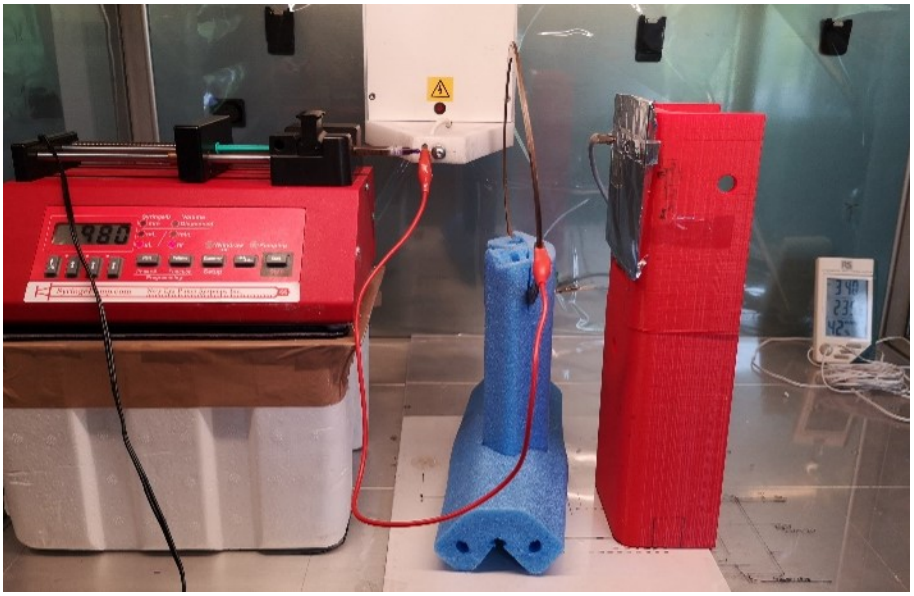

Figure B.1: Electrospray setup

C GZO Results

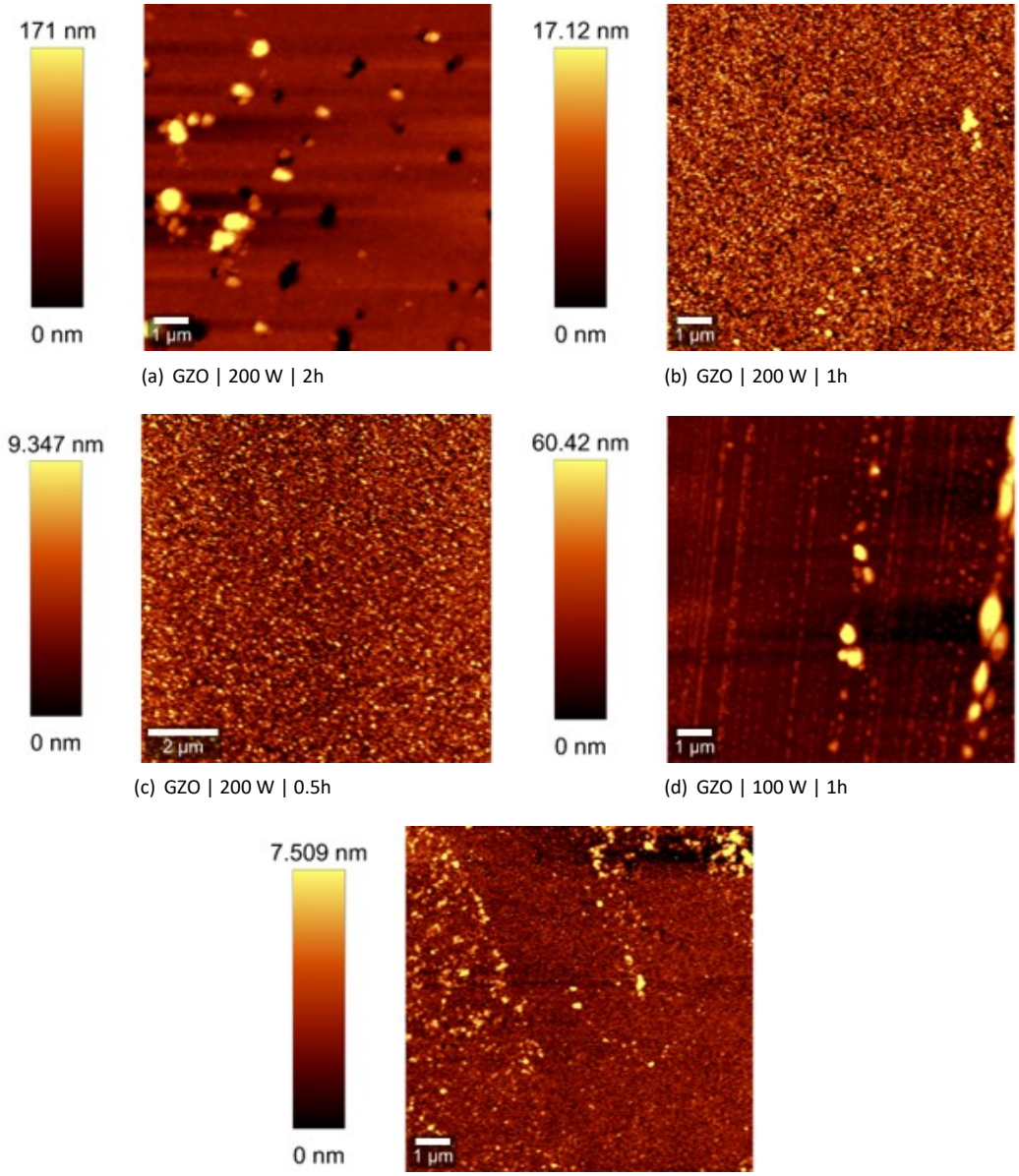

(a) GZO | 200 W | 2h

(b) GZO | 200 W | 1h

(c) GZO | 200 W | 0.5h

(d) GZO | 100 W | 1h

(e) GZO | 50 W | 1h

Figure C.1: AFM images of GZO films

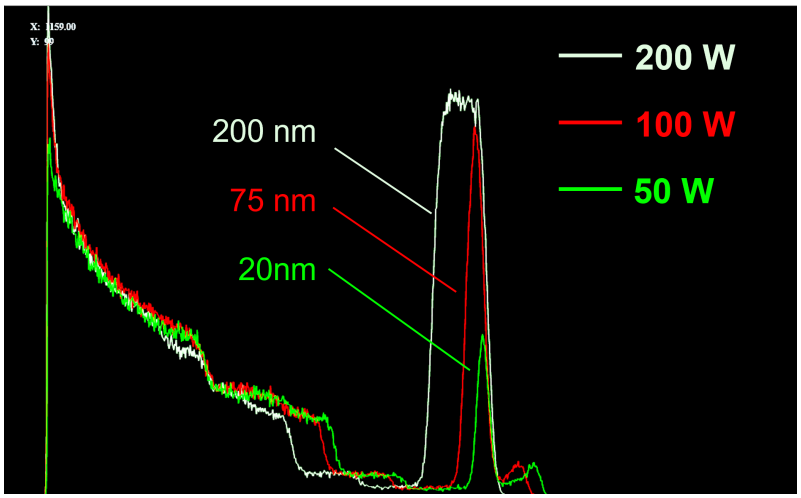

(a) 1 h deposition

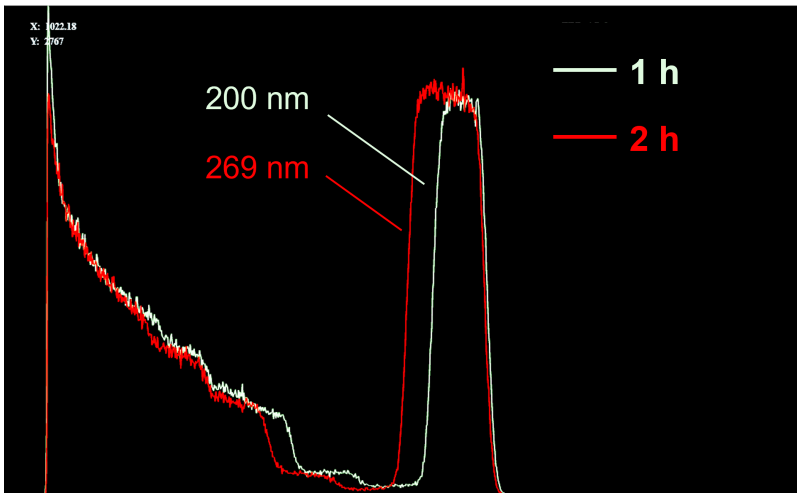

(b) 200 W deposition

Figure C.2: RBS results

Table C.1: GZO roughness and thickness values

Sputtering conditions Power / W	Time / h	Roughness / nm	Thickness / nm	Bandgap / eV
200	2	39.2 22.9 48	275 262-271	3.12
200	1	5 4	200	3.18
200	0.5	2 2.3 1.9 1.5	77-80	3.29
100	1	9.4 9	75	3.37
50	1	5.5 1.5	20	3.88

D Bandgap of Sulfide Films

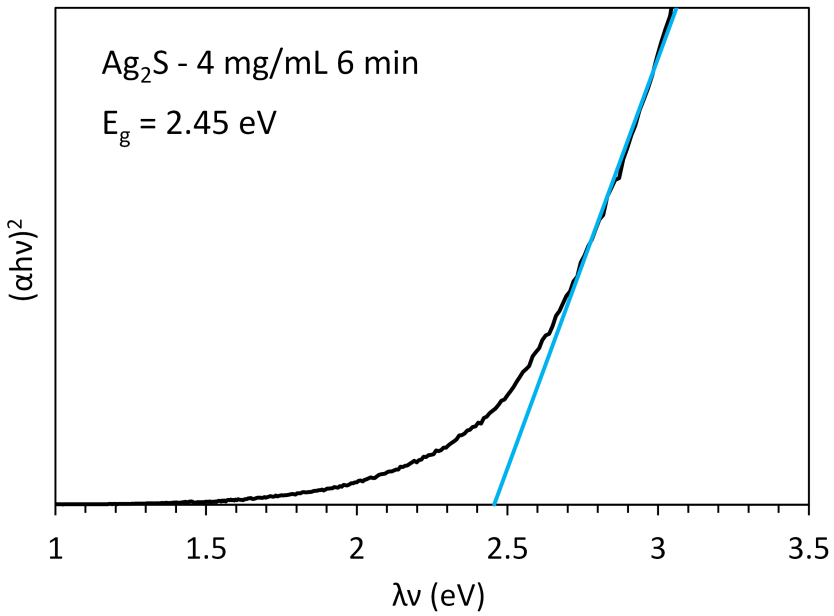

(a) Ag_2S

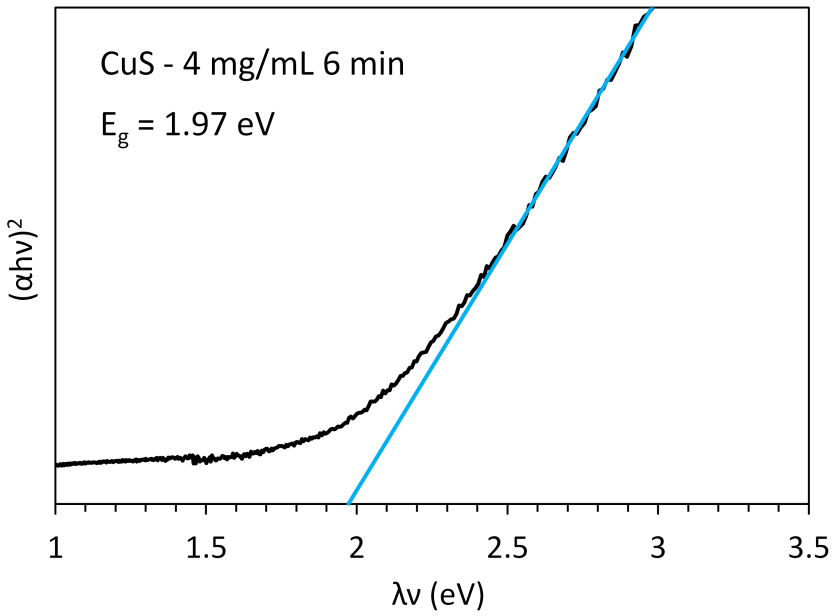

(b) CuS

Figure D.1: Bandgap of sulfide films